Engineering with Computers (2021) 37:1657–1678
https://doi.org/10.1007/s00366-021-01303-z

ORIGINAL ARTICLE

Size-dependent nonlinear bending behavior of porous FGM quasi-3D microplates with a central cutout based on nonlocal strain gradient isogeometric finite element modelling

Shan-Xiang Chen[1] · Saeid Sahmani[2] · Babak Safaei[3]

Received: 17 October 2020 / Accepted: 16 January 2021 / Published online: 4 February 2021

Abstract

With the aid of the non-uniform rational B-spline (NURBS)-based isogeometric technique, for the first time, the size-dependent geometrically nonlinear bending characteristics of microplates made of porous functionally graded materials (FGMs) having a central cutout with different shapes are studied. The nonlocal strain gradient continuum elasticity within the framework a hybrid higher-order quasi-3D plate theory is adopted to describe the kinematic relations via only four unknowns. To capture the effective material properties, a porosity-dependent rule of mixture is employed. The nonlocal strain gradient nonlinear load–deflection responses are obtained corresponding to various geometrical and material parameters as well as different boundary conditions. It is revealed that the significance of both the nonlocal and strain gradient reduces. This prediction is the same for all values of the material property gradient index as well as the porosity index. Also, it is demonstrated that a central cutout leads to change the trend of load–deflection response, and this change occurs at a specific value for the applied distributed load which depends on several parameters such as the cutout geometry and boundary conditions. In addition, it is displayed that corresponding to different maximum deflections, the significance of the strain gradient size effect in the absence of nonlocality on the nonlinear flexural stiffness of a porous FGM microplate is more than that of the nonlocal size effect in the absence of the strain gradient size dependency.

Keywords Non-classical continuum elasticity · Quasi-3D theory · Isogeometric finite element method · Nonlocality · Porous composite material · Strain gradient size dependency

1 Introduction

Recently, through advancement of materials science and technology, porous structures have been manufactured to develop lightweight as well as controlled pore systems with desired mechanical properties and functionality. Accordingly, several investigations have been carried out. Cheng et al. [1] presented a study on the multifaceted applications of cellulosic porous materials in environment, health and energy. Wang et al. [2] presented a review study on the photocatalytic and electrocatalytic applications of two-dimensional porous materials. Guo et al. [3] employed the microwave cavity interference enhancement technique to image nano-defects in porous materials putting the metal waveguides to use. Zhang et al. [4] prepared nitrogen-doped hierarchical porous carbon materials with the aid of a template free method for application in CO_2 capture. Yu et al. [5] fabricated porous carbon materials using corn straw as anode materials for lithium ion batteries. Safaei [6] explored the effect of embedding a porous core on the free oscillation response of a sandwich composite plate. Gao et al. [7] and Moradi-Dastjerdi et al. [8] analyzed, respectively, the wave propagation and static performance of porous plates reinforced with carbon nanotubes. Lin et al. [9] introduced an antibacterial, thermo and light-responsive porous composite material having smart titanium particles.

✉ Saeid Sahmani
s.sahmani@ug.edu.ge

✉ Babak Safaei
babak.safaei@emu.edu.tr

1 School of Traffic and Transportation Engineering, Changsha University of Science and Technology, Changsha 41004, Hunan, China

2 School of Science and Technology, The University of Georgia, 0171 Tbilisi, Georgia

3 Department of Mechanical Engineering, Eastern Mediterranean University, Famagusta, North Cyprus via Mersin 10, Turkey

To capture the influences of different small scale effects, it is necessary to implement them into the classical continuum elasticity. Accordingly, various non-classical continuum elasticity theories have been introduced to accomplish this purpose. In the last two decades, several investigations have been carried out to analyze size-dependent mechanical behaviors of structures having small scaled dimensions [10–28]. To mention some recent studies in this field, Li et al. [29] developed a size-dependent inhomogeneous beam model accounting the through-length variation of material properties for nonlocal strain gradient Euler–Bernoulli beams made of axially functionally graded material (FGM). Nguyen et al. [30] introduced a refined quasi-3D isogeometric analysis for FGM microplates having seventh-order shear deformation including couple stress size effect. Joshi et al. [16] considered the temperature effect on vibration response of cracked Kirchhoff FGM microplates on the basis of the strain gradient elasticity. Radic and Jeremic [31] explored the vibration and buckling behaviors of orthotropic double-layered graphene sheets subjected to hygrothermal loading on the basis of the differential form of nonlocal theory of elasticity. Sahmani and Aghdam [32–34] constructed nonlocal hybrid FGM shell models to predict nonlinear static instability of cylindrical nanoshells under various loading conditions. Al-Shujairi and Mollamahmutoglu [35] constructed nonlocal strain gradient beam model for buckling and free vibrations of FGM sandwich microbeams in thermal environments. Jia et al. [36] investigated the thermos-electro-mechanical buckling behavior of FGM composite microbeams based upon the modified couple stress theory of elasticity. Thanh et al. [37] predicted static and free vibrations of couple stress-based FGM carbon nanotube reinforced composite nanoplates. Taati [38] examined buckling and postbuckling responses of FGM composite modified couple stress-based microbeams. Hajmohammad et al. [39] studied bending and buckling characteristics of FGM composite annular microplates with piezoelectric facesheet within the framework of the nonlocal continuum elasticity. Soleimani and Tadi Beni [40] reported an axisymmetric shell element formulation with the aid of a two node shell element incorporating couple stress type of size dependency.

To mention some more recent studies, Ghorbani Shenas et al. [41] analyzed thermal prebuckling and postbuckling of pre-twisted rotating FGM composite microbeams subjected to a thermal environment on the basis of the modified strain gradient continuum elasticity. Sahmani et al. [42–45] anticipated the nonlinear free and forced vibrations of FGM nanoshells incorporating modal interactions in the presence of surface stress size effect. Sobhy and Zenkour [46] explored the influences of porosity and inhomogeneity on the size-dependent buckling and oscillations of FGM composite quasi-3D nanoplates. Phung-Van et al. [47] studied the porosity-dependent nonlinear transient responses of FGM nanoplates in the presence of nonlocal type of size effect. Aria and Friswell [48] investigated the hygro-thermal vibration and buckling responses of FGM sandwich temperature-dependent microbeams. Jun et al. [49] proposed a modified nonlocal elasticity theory incorporating much more general constitutive equations containing three characteristics lengths to analyze buckling behavior of nanobeams. Sahmani and Safaei [50–52] studied size-dependent nonlinear mechanical responses of bi-directional FGM nanobeams. Thai et al. [53] introduced a modified strain gradient-based computational model for free vibration behavior of FGM composite multilayer microplates. Thanh et al. [54] utilized the modified couple stress elasticity for thermal bending and buckling of composite laminate microplates. Fang et al. [55] constructed a new nonlocal Euler–Bernoulli beam model for vibrations and thermal buckling of FGM composite nanobeams in thermal environment. Yuan et al. [56–58] employed different size-dependent continuum theories to investigate nonlinear behaviors of FGM truncated conical microshells. Sarthak et al. [59] studied dynamic buckling of curved nanobeams with the aid of nonlinear nonlocal finite element method together with a higher-order shear flexible plate model. Thai et al. [60] developed a size-dependent Kriging meshfree model to analyze deformation as well as free vibrations of FGM carbon nanotube reinforced nanobeams. Zhang et al. [61] employed a two-node strain gradient Reddy beam element for static and dynamic analysis of microbeams. Sahmani and Safaei [62] presented a surface elastic-based conical shell model for nonlinear vibration characteristics of FGM conical nanoshells. The size-dependent shear buckling characteristics of FGM skew nanoplates are analyzed by Fam et al. [63], and Yuan et al. [64]. Karamanli and Vo [65] carried out a study on bending, buckling and free vibrations of FGM sandwich microbeams based on the modified strain gradient elasticity theory. Fan et al. [66] investigated the dynamic stability of conical microshells surrounded by a viscoelastic medium based on the couple stress elasticity. Guo et al. [67] reported the three-dimensional nonlocal buckling loads of composite nanoplates with coated one-dimensional quasicrystal. Ghane et al. [68] conducted a flutter instability analysis of fluid-conveying nanotubes under an external magnetic field based upon the nonlocal strain gradient Timoshenko beam model. Mao et al. [69] explored the free vibration response of FGM piezoelectric composite microplates within the framework of the nonlocal continuum elasticity. Thanh et al. [70] introduced a geometrically nonlinear size-dependent plate model for porous FGM microplates based on the modified couple stress theory. Fan et al. [71–73] employed the isogeometric method for size-dependent nonlinear responses of porous FGM microplates.

In the current study, through combination of the nonlocal strain gradient continuum elasticity and a hybrid-type quasi-3D plate theory, the size-dependent geometrically nonlinear flexural behavior of porous FGM microplates having a central cutout with different shapes is investigated. The material properties of microplates are approximated via a porosity-dependent rule of mixture. With the aid of the NURBS-based isogeometric approach, the possibility of flexibly meeting higher-order derivatives is achieved. Several case studies including various porosity dispersion patterns, different material gradient indexes, boundary conditions, and shapes of the central cutout are presented.

2 Quasi-3D nonlocal strain gradient porous FGM plate model

In the current investigation, typical rectangular microplates having a central cutout made of a porous functionally graded material (FGM) are taken into consideration. To this purpose, three different kinds of porous distribution scheme are supposed as shown schematically in Fig. 1. Accordingly, a porosity-dependent rule of mixture is employed to estimate the material fulfilling the partition of unity in the following form [74]

$$\mathcal{P}(z) = \mathcal{P}_c\left[\left(\frac{1}{2}+\frac{z}{h}\right)^k - \frac{\Gamma}{2}\right] + \mathcal{P}_m\left[1 - \left(\frac{1}{2}+\frac{z}{h}\right)^k - \frac{\Gamma}{2}\right], \tag{1}$$

in which Γ and k are the porosity index and the material property gradient index, respectively.

Consequently, the effective Young's modulus and Poisson's ratio of porous FGM microplates relevant to each kind of the porosity dispersion scheme can be extracted based on the porosity-dependent rule of mixture as

$$E(z) = \left(E_c - E_m\right)\varphi_1(z) + E_m - \left(E_c + E_m\right)\Gamma\varphi_2(z), \tag{2a}$$

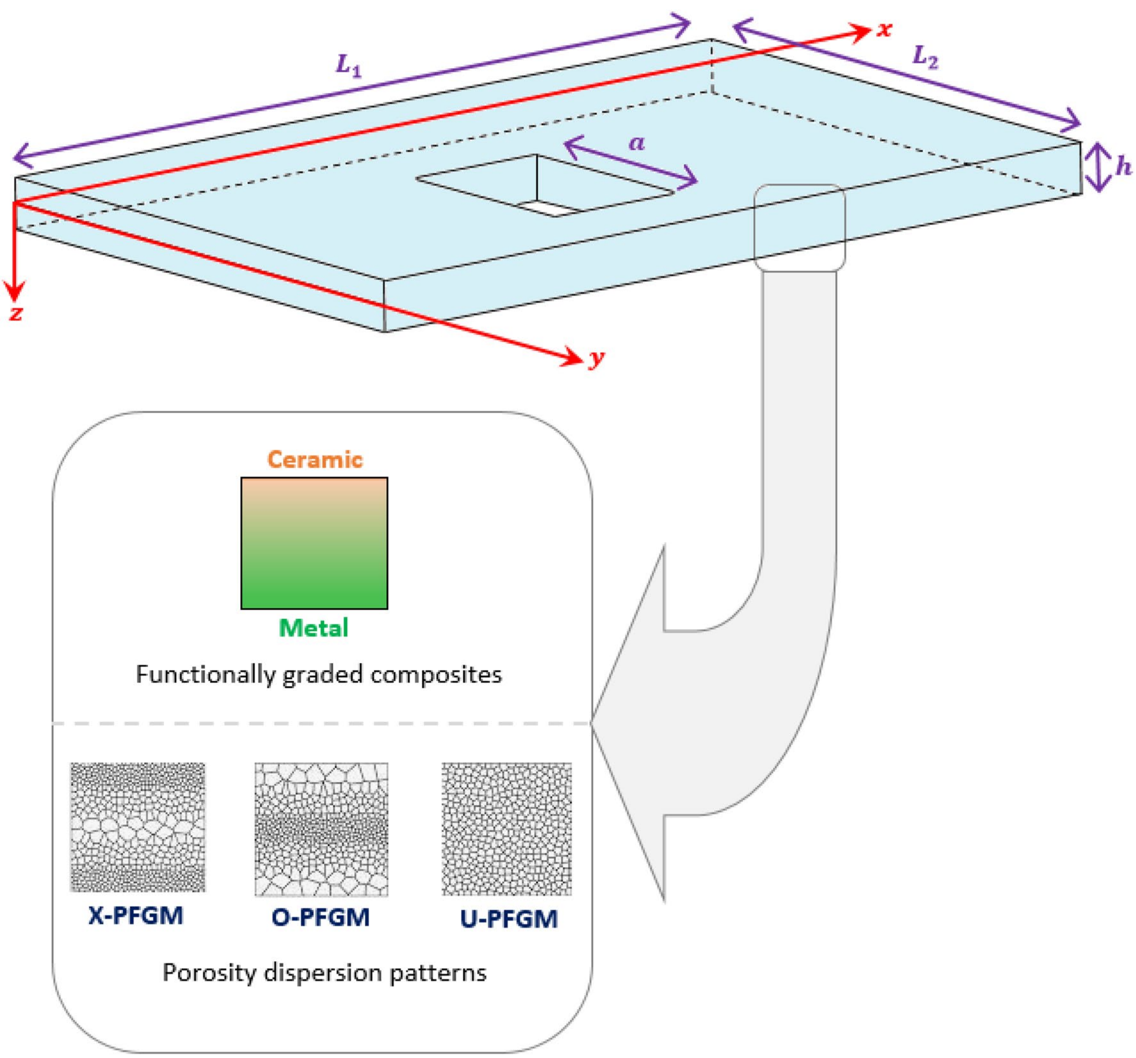

Fig. 1 Illustration schematically a porous FGM microplate having a central cutout

$$\nu(z) = \left(\nu_{\mathrm{c}} - \nu_{\mathrm{m}}\right)\varphi_1(z) + E_{\mathrm{m}} - \left(\nu_{\mathrm{c}} + \nu_{\mathrm{m}}\right)\Gamma\varphi_2(z), \tag{2b}$$

where,

$$\varphi_1(z) = \left(\frac{1}{2} + \frac{z}{h}\right)^k, \quad \varphi_2(z) = \begin{cases} \frac{1}{2} & \text{U-PFGM} \\ \frac{1}{2} - \frac{|z|}{h} & \text{O-PFGM} \\ -\frac{|z|}{h} & \text{X-PFGM} \end{cases} \tag{3}$$

In Figs. 2, 3 and 4, the variation of the dimensionless effective Young's modulus ($E(z)/E_c$) through the plate thickness and porosity index of porous FGM microplates are plotted corresponding to different values of the material property gradient index.

Within the framework of a higher-order shear deformation plate theory, the displacement field can be expressed as

$$\mathcal{U}_x(x,y,z) = u(x,y) - z\frac{\partial w(x,y)}{\partial x} + \mathbb{f}(z)\left(\psi_x(x,y) + \frac{\partial w(x,y)}{\partial x}\right), \tag{4a}$$

$$\mathcal{U}_y(x,y,z) = v(x,y) - z\frac{\partial w(x,y)}{\partial y} + \mathbb{f}(z)\left(\psi_y(x,y) + \frac{\partial w(x,y)}{\partial y}\right), \tag{4b}$$

$$\mathcal{U}_z(x,y,z) = w(x,y), \tag{4c}$$

in which u, v, w are the mid-plane displacement variables along x, y, and z axes, respectively. Also, ψ_x, ψ_y are the rotations about y-axis and x-axis, respectively. $\mathbb{f}(z)$ represents the transverse shear shape function to take shear deformation into account.

By separating the transverse displacement variable into the bending and shear components, and implementing the transverse normal shape function $\mathbb{g}(z)$ to take the normal

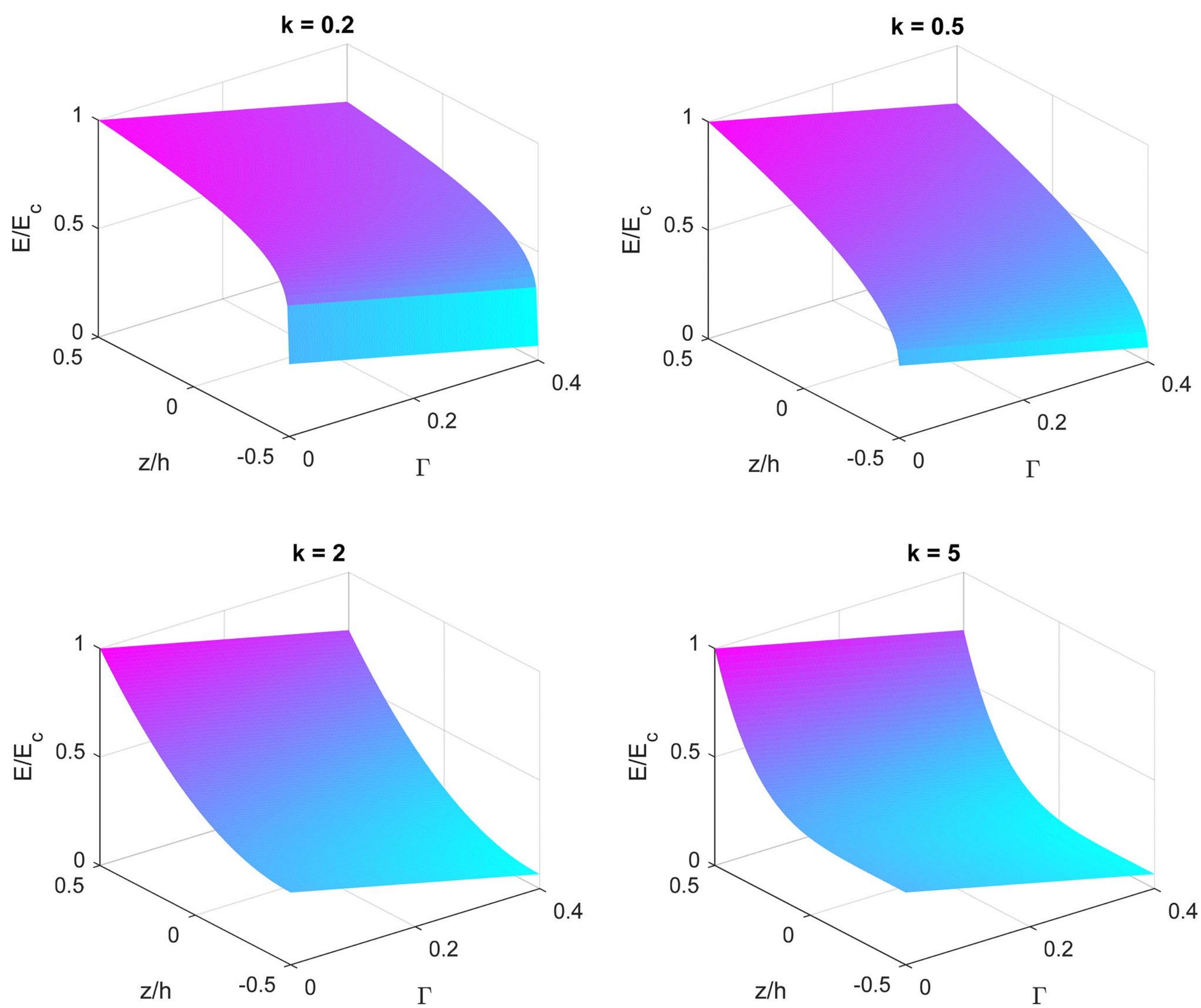

Fig. 2 Variation of Young's modulus of a U-PFGM microplate with porosity index and through thickness corresponding to different material property gradient indexes

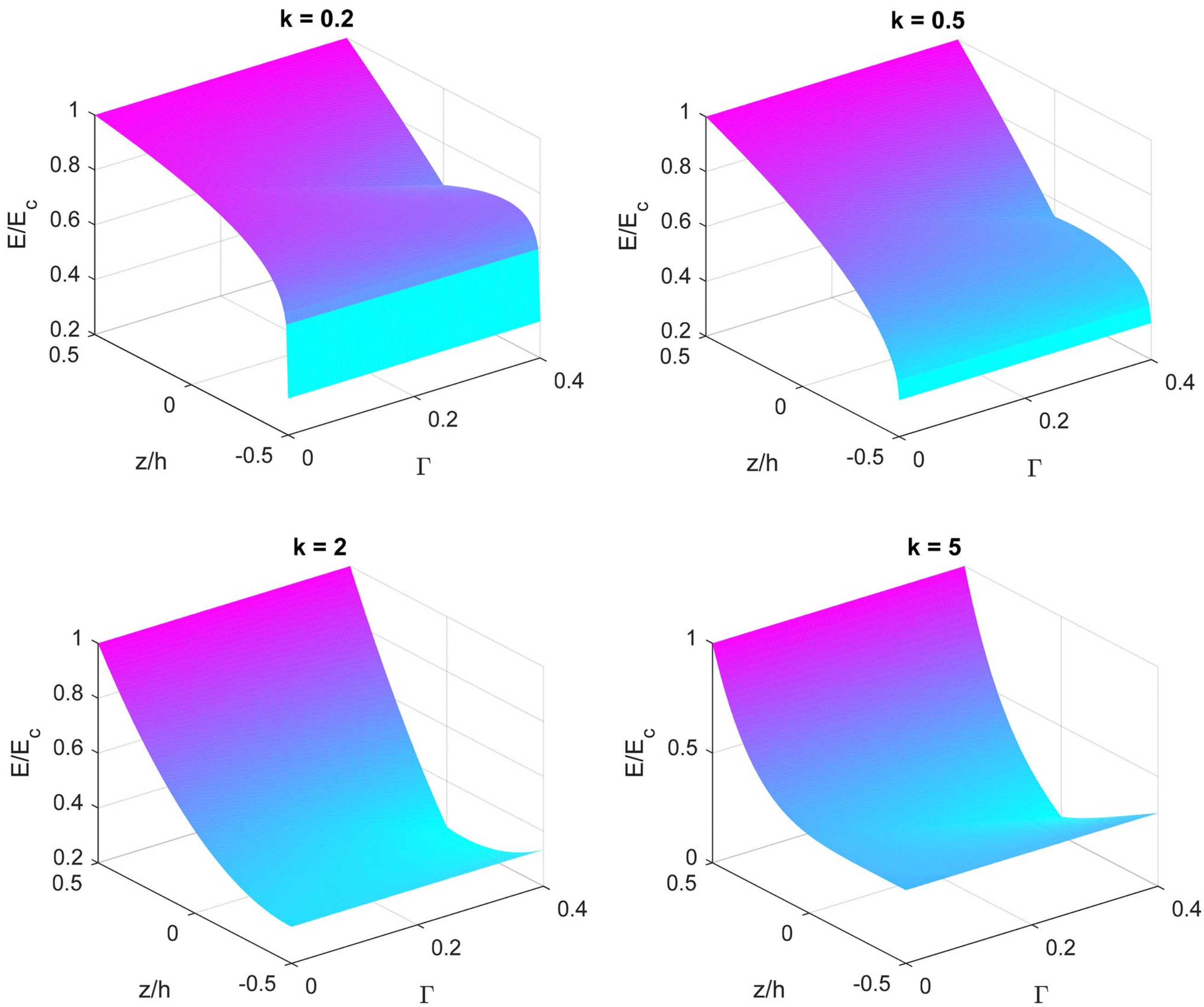

Fig. 3 Variation of Young's modulus of an O-PFGM microplate with porosity index and through thickness corresponding to different material property gradient indexes

strains through the thickness into consideration, one will have

$$\mathcal{U}_x(x,y,z) = u(x,y) - z\frac{\partial w_b(x,y)}{\partial x} + (\mathbb{f}(z) - z)\frac{\partial w_s(x,y)}{\partial x}, \quad (5a)$$

$$\mathcal{U}_y(x,y,z) = v(x,y) - z\frac{\partial w_b(x,y)}{\partial y} + (\mathbb{f}(z) - z)\frac{\partial w_s(x,y)}{\partial y}, \quad (5c)$$

$$\mathcal{U}_z(x,y,z) = w_b(x,y) + (1 + \mathbb{g}(z))w_s(x,y), \quad (5c)$$

where $w_b(x,y)$ and $w_s(x,y)$ denote, respectively, the bending and shear displacement variables. By assuming a sinusoidal shear function for $\mathbb{f}(z)$, and a trigonometric shape function for $\mathbb{g}(z)$, the hybrid-type quasi-3D higher-order shear deformation theory can be achieved. So, it is supposed that

$$\mathbb{F}(z) = \sin\left(\frac{\pi z}{h}\right) - z, \quad (6a)$$

$$\mathbb{G}(z) = 1 + \frac{5}{12\pi}\cos\left(\frac{\pi z}{h}\right), \quad (6b)$$

Figure 5 demonstrates the through-thickness profiles of the introduced shape functions and their derivatives.

Now, the strain–displacement equations including the von-Karman geometric nonlinearity can be written within the developed hybrid-type quasi-3D higher-order shear deformation theory as below

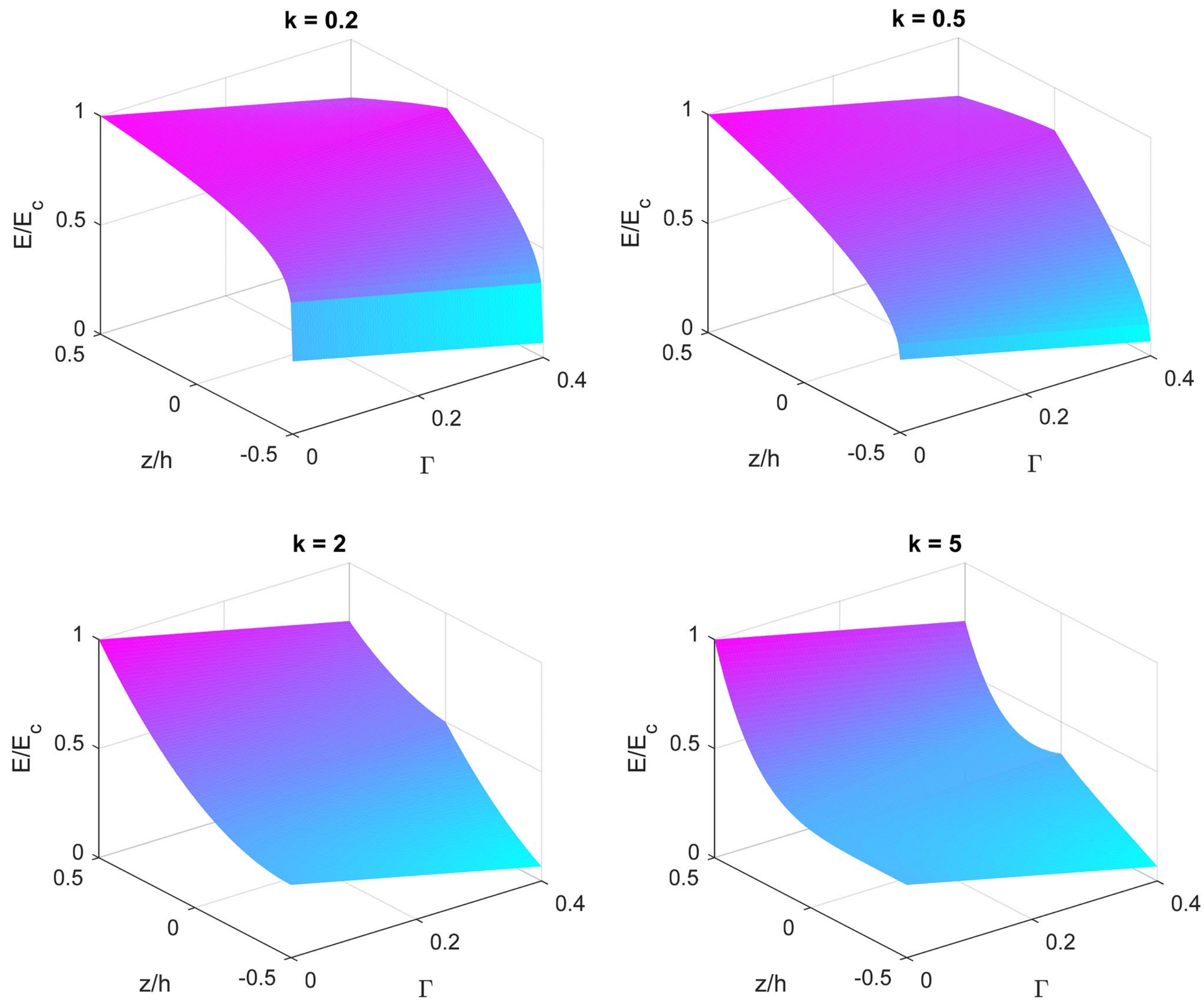

Fig. 4 Variation of Young's modulus of a X-PFGM microplate with porosity index and through thickness corresponding to different material property gradient indexes

$$
\begin{aligned}
\varepsilon_{xx} &= \frac{\partial u}{\partial x} + \frac{1}{2}\left(\frac{\partial w_b}{\partial x} + \frac{\partial w_s}{\partial x}\right)^2 - z\frac{\partial^2 w_b}{\partial x^2} + \mathbb{F}(z)\frac{\partial^2 w_s}{\partial x^2}\\
\varepsilon_{yy} &= \frac{\partial v}{\partial y} + \frac{1}{2}\left(\frac{\partial w_b}{\partial y} + \frac{\partial w_s}{\partial y}\right)^2 - z\frac{\partial^2 w_b}{\partial y^2} + \mathbb{F}(z)\frac{\partial^2 w_s}{\partial y^2}\\
\varepsilon_{zz} &= \frac{\mathrm{d}\mathbb{G}(z)}{\mathrm{d}z} w_s\\
\gamma_{xy} &= \frac{\partial u}{\partial y} + \frac{\partial v}{\partial x} + \left(\frac{\partial w_b}{\partial x} + \frac{\partial w_s}{\partial x}\right)\left(\frac{\partial w_b}{\partial y} + \frac{\partial w_s}{\partial y}\right) - 2z\frac{\partial^2 w_b}{\partial x \partial y} + 2\mathbb{F}(z)\frac{\partial^2 w_s}{\partial x \partial y}\\
\gamma_{xz} &= \left(\frac{\mathrm{d}\mathbb{F}(z)}{\mathrm{d}z} + \mathbb{G}(z)\right)\frac{\partial w_s}{\partial x}\\
\gamma_{yz} &= \left(\frac{\mathrm{d}\mathbb{F}(z)}{\mathrm{d}z} + \mathbb{G}(z)\right)\frac{\partial w_s}{\partial y}.
\end{aligned}
\tag{7}
$$

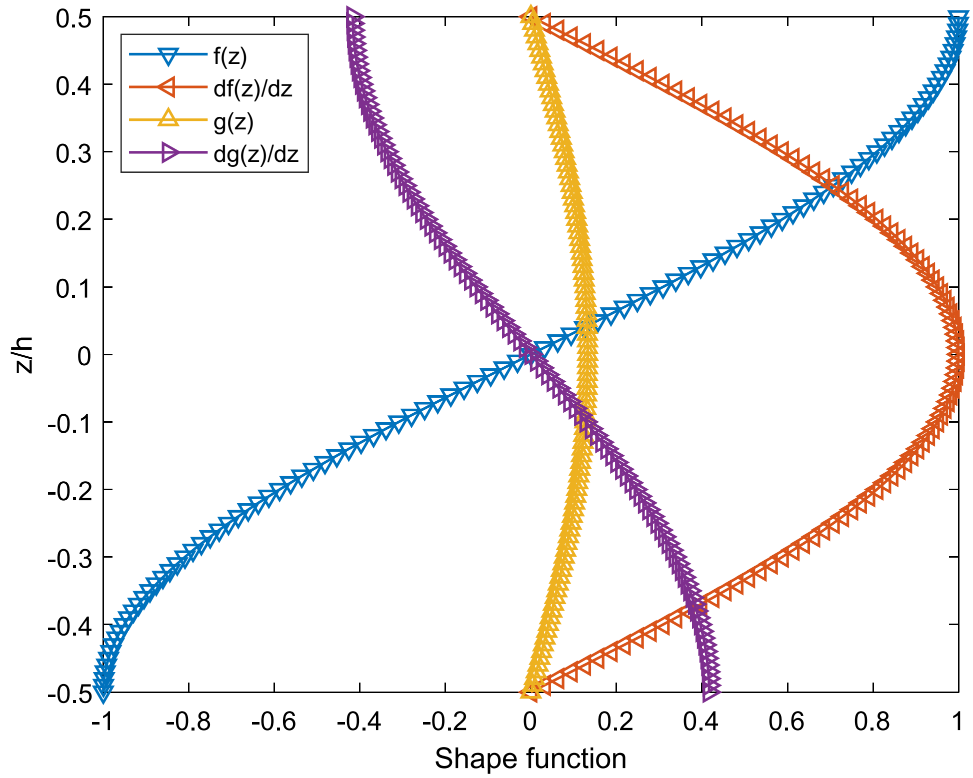

Fig. 5 Variation of shape functions and their derivatives through plate thickness considered for the developed hybrid higher-order quasi-3D plate model

Accordingly, the stress–strain constitutive equations can be expressed in the following form

$$\begin{Bmatrix} \sigma_{xx} \\ \sigma_{yy} \\ \sigma_{zz} \\ \tau_{xy} \\ \tau_{yz} \\ \tau_{xz} \end{Bmatrix} = \begin{bmatrix} Q_{11}(z) & Q_{12}(z) & Q_{13}(z) & 0 & 0 & 0 \\ Q_{12}(z) & Q_{22}(z) & Q_{23}(z) & 0 & 0 & 0 \\ Q_{13}(z) & Q_{23}(z) & Q_{33}(z) & 0 & 0 & 0 \\ 0 & 0 & 0 & Q_{44}(z) & 0 & 0 \\ 0 & 0 & 0 & 0 & Q_{55}(z) & 0 \\ 0 & 0 & 0 & 0 & 0 & Q_{66}(z) \end{bmatrix} \begin{Bmatrix} \varepsilon_{xx} \\ \varepsilon_{yy} \\ \varepsilon_{zz} \\ \gamma_{xy} \\ \gamma_{yz} \\ \gamma_{xz} \end{Bmatrix}, \tag{8}$$

where,

$$\begin{aligned} Q_{11}(z) &= Q_{22}(z) = Q_{33}(z) = \frac{(1-\nu(z))E(z)}{(1-2\nu(z))(1+\nu(z))}, \\ Q_{12}(z) &= Q_{13}(z) = Q_{23}(z) = \frac{\nu(z)E(z)}{(1-2\nu(z))(1+\nu(z))}, \\ Q_{44}(z) &= Q_{55}(z) = Q_{66}(z) = \frac{E(z)}{2(1+\nu(z))}. \end{aligned} \tag{9}$$

On the basis of the nonlocal strain gradient continuum elasticity, the total stress tensor can be expressed as follows [75]

$$\Phi_{ij} = \sigma_{ij} - \nabla\sigma^*_{ijm}, \tag{10}$$

where the classical and higher-order stresses can be defined, respectively, as below,

$$\sigma_{ij} = \int_V \chi_1\left(x', x, e_1\right) C_{ijkl}\varepsilon_{kl}\mathrm{d}V, \tag{11a}$$

$$\sigma^*_{ijm} = l^2 \int_V \chi_2\left(x', x, e_2\right) C_{ijkl}\varepsilon_{kl,m}\mathrm{d}V, \tag{11b}$$

in which e_1 and e_2 represent the nonlocal parameters regarding the size effect of the nonlocal stress. Also l denotes the material length scale parameter to take the strain gradient size dependency into account. ε_{kl}, $\varepsilon_{kl,m}$ and C_{ijkl} are the strain components, strain gradient components and elastic coefficients. In accordance with nonlocal strain gradient theory, it is assumed that the two kernel functions of $\chi_1\left(x', x, e_1\right)$ and $\chi_2\left(x', x, e_2\right)$ should satisfy the associated conditions introduced by Eringen [76] as follow

$$\sigma_{ij} - e_1^2\left(\frac{\partial^2\sigma_{ij}}{\partial x^2} + \frac{\partial^2\sigma_{ij}}{\partial y^2}\right) = C_{ijkl}\varepsilon_{kl}, \tag{12a}$$

$$\sigma^*_{ijm} - e_2^2\left(\frac{\partial^2\sigma^*_{ijm}}{\partial x^2} + \frac{\partial^2\sigma^*_{ijm}}{\partial y^2}\right) = l^2 C_{ijkl}\varepsilon_{kl,m}. \tag{12b}$$

As a result, the generalized constitutive equation on the basis of the nonlocal strain gradient elasticity can be written as

$$\left[1-e_1^2\left(\frac{\partial^2}{\partial x^2}+\frac{\partial^2}{\partial y^2}\right)\right]\left[1-e_2^2\left(\frac{\partial^2}{\partial x^2}+\frac{\partial^2}{\partial y^2}\right)\right]\Phi_{ij} = \left[1-e_1^2\left(\frac{\partial^2}{\partial x^2}+\frac{\partial^2}{\partial y^2}\right)\right]C_{ijkl}\varepsilon_{kl} - l^2\left[1-e_2^2\left(\frac{\partial^2}{\partial x^2}+\frac{\partial^2}{\partial y^2}\right)\right]C_{ijkl}\frac{\partial^2\varepsilon_{kl}}{\partial x^2} \tag{13}$$

With assumption of $e_1 = e_2 = e$, one will have

$$\Phi_{ij} - e^2\left(\frac{\partial^2\Phi_{ij}}{\partial x^2}+\frac{\partial^2\Phi_{ij}}{\partial y^2}\right) = C_{ijkl}\varepsilon_{kl} - l^2 C_{ijkl}\left(\frac{\partial^2\varepsilon_{kl}}{\partial x^2}+\frac{\partial^2\varepsilon_{kl}}{\partial y^2}\right).$$

Accordingly, the variation of the strain energy for a porous FGM microplate modeled via the nonlocal strain gradient hybrid-type quasi-3D higher-order shear deformation theory can be expressed as

$$\delta\Pi_S = \int_S \int_{-\frac{h}{2}}^{\frac{h}{2}} \Phi_{ij}\delta\varepsilon_{ij}\mathrm{d}z\mathrm{d}S, \tag{15}$$

Also, the virtual work caused by the external distributed load q can be written as

$$\delta\Pi_W = \int_S \delta w \mathrm{d}S, \tag{16}$$

On the basis of the virtual work principle, and through substituting Eqs. (7) and (8) into Eq. (15), one will have

$$\int_S \left\{\delta\left(\mathfrak{P}_b^T\right)\boldsymbol{\xi}_b\mathfrak{P}_b - l^2\delta\left(\nabla^2\mathfrak{P}_b^T\right)\boldsymbol{\xi}_b\mathfrak{P}_b + \delta\left(\mathfrak{P}_s^T\right)\boldsymbol{\xi}_s\mathfrak{P}_s - l^2\delta\left(\nabla^2\mathfrak{P}_s^T\right)\boldsymbol{\xi}_s\mathfrak{P}_s\right\}\mathrm{d}S = \int_S \left(1-e^2\nabla^2\right)\delta w\mathrm{d}S, \tag{17}$$

in which

$$\mathfrak{P}_b = \begin{bmatrix} \frac{\partial u}{\partial x}+\frac{1}{2}\left(\frac{\partial w_b}{\partial x}+\frac{\partial w_s}{\partial x}\right)^2 & -\frac{\partial^2 w_b}{\partial x^2} & \frac{\partial^2 w_s}{\partial x^2} & 0 \\ \frac{\partial v}{\partial y}+\frac{1}{2}\left(\frac{\partial w_b}{\partial y}+\frac{\partial w_s}{\partial y}\right)^2 & -\frac{\partial^2 w_b}{\partial y^2} & \frac{\partial^2 w_s}{\partial y^2} & 0 \\ \frac{\partial u}{\partial y}+\frac{\partial v}{\partial x}+\left(\frac{\partial w_b}{\partial x}+\frac{\partial w_s}{\partial x}\right)\left(\frac{\partial w_b}{\partial y}+\frac{\partial w_s}{\partial y}\right) & -2\frac{\partial^2 w_b}{\partial x\partial y} & 2\frac{\partial^2 w_s}{\partial x\partial y} & 0 \\ 0 & 0 & 0 & w_s \end{bmatrix}^T$$
$$\boldsymbol{\xi}_b = \begin{bmatrix} A_b & B_b & C_b & E_b \\ B_b & D_b & F_b & G_b \\ C_b & F_b & H_b & K_b \\ E_b & G_b & K_b & J_b \end{bmatrix},\quad \mathfrak{P}_s = \begin{bmatrix} \frac{\partial w_s}{\partial x} \\ \frac{\partial w_s}{\partial y} \end{bmatrix},\quad \boldsymbol{\xi}_s = \int_{-\frac{h}{2}}^{\frac{h}{2}} \left(\frac{\mathrm{d}\mathbb{F}(z)}{\mathrm{d}z}+\mathbb{G}(z)\right)^2 \begin{bmatrix} Q_{44}(z) & 0 \\ 0 & Q_{55}(z) \end{bmatrix}\mathrm{d}z \tag{18}$$

where,

$$\left\{A_b, B_b, C_b\right\} = \int_{-\frac{h}{2}}^{\frac{h}{2}} \{1, z, \mathbb{F}(z)\} \begin{bmatrix} Q_{11}(z) & Q_{12}(z) & 0 & Q_{13}(z) \\ Q_{12}(z) & Q_{22}(z) & 0 & Q_{23}(z) \\ 0 & 0 & Q_{66}(z) & 0 \\ Q_{31}(z) & Q_{32}(z) & 0 & Q_{33}(z) \end{bmatrix}\mathrm{d}z$$
$$\left\{D_b, E_b, F_b, G_b\right\} = \int_{-\frac{h}{2}}^{\frac{h}{2}} \left\{z^2, \frac{\mathrm{d}\mathbb{G}(z)}{\mathrm{d}z}, z\mathbb{F}(z), z\frac{\mathrm{d}\mathbb{G}(z)}{\mathrm{d}z}\right\} \begin{bmatrix} Q_{11}(z) & Q_{12}(z) & 0 & Q_{13}(z) \\ Q_{12}(z) & Q_{22}(z) & 0 & Q_{23}(z) \\ 0 & 0 & Q_{66}(z) & 0 \\ Q_{31}(z) & Q_{32}(z) & 0 & Q_{33}(z) \end{bmatrix}\mathrm{d}z \tag{19}$$
$$\left\{H_b, K_b, J_b\right\} = \int_{-\frac{h}{2}}^{\frac{h}{2}} \left\{\mathbb{F}^2(z), \mathbb{F}(z)\frac{\mathrm{d}\mathbb{G}(z)}{\mathrm{d}z}, \left(\frac{\mathrm{d}\mathbb{G}(z)}{\mathrm{d}z}\right)^2\right\} \begin{bmatrix} Q_{11}(z) & Q_{12}(z) & 0 & Q_{13}(z) \\ Q_{12}(z) & Q_{22}(z) & 0 & Q_{23}(z) \\ 0 & 0 & Q_{66}(z) & 0 \\ Q_{31}(z) & Q_{32}(z) & 0 & Q_{33}(z) \end{bmatrix}\mathrm{d}z$$

3 Isogeometric solution methodology

The isogeometric numerical solving process has been widely use in recent years [77–88]. Within a one-dimensional domain, the associated knot vector can be expressed in a non-decreasing form as below:

$$\mathbb{K}(\xi) = \left\{\xi_1, \xi_2, \xi_3, \ldots, \xi_{m+n+1}\right\}, \tag{20}$$

where m and n stand for the number of basis function and the order of the B-spline basis function. In addition, it is necessary that each ith knot satisfies the condition of $0 \leq \xi_i \leq 1$. As a consequence, the B-spline basis function is written based on the recursive Cox–de Boor formula as below

$$\mathcal{X}_{i,0}(\xi) = \begin{cases} 1 & \xi_i \leq \xi < \xi_{i+1} \\ 0 & \text{else,} \end{cases} \tag{21a}$$

$$\mathcal{X}_{i,n}(\xi) = \frac{\xi - \xi_i}{\xi_{i+n} - \xi_i}\mathcal{X}_{i,n-1}(\xi) + \frac{\xi_{i+n+1} - \xi}{\xi_{i+n+1} - \xi_{i+1}}\mathcal{X}_{i+1,n-1}(\xi), \tag{21b}$$

Within a two-dimensional domain, the tensor product of two basic functions can be utilized to achieve the associated B-spline basis function as follows

$$\mathcal{F}_{i,j}^{p,q}(\xi, \eta) = \sum_{i=1}^{m} \mathfrak{J}_i(x, y)\mathcal{P}_i, \tag{22}$$

where $\mathcal{P}_i$ denote the control points within the bi-directional control net, and

$$\mathfrak{J}_i(\xi, \eta) = \frac{\mathcal{X}_{i,p}(\xi)\mathcal{X}_{j,q}(\eta)\mathfrak{W}_{i,j}}{\sum_{i=1}^{m}\sum_{j=1}^{n}\mathcal{X}_{i,p}(\xi)\mathcal{X}_{j,q}(\eta)\mathfrak{W}_{i,j}}, \tag{23}$$

in which $\mathcal{X}_{i,p}(\xi)$ and $\mathcal{X}_{j,q}(\eta)$ represent, respectively, the shape functions of orders p and q along ξ and η directions. Also, $\mathfrak{W}_{i,j}$ is the relevant weight coefficient. Thereafter, the knot vector of $\mathbb{K}(\eta)$ is employed to extract the derivation of the shape function $\mathcal{X}_{j,q}(\eta)$. In Fig. 6, the considered cubic elements for square microplates with and without a central cutout are illustrated.

By taking the non-uniform rational B-spline (NURBS)-based isogeometric analysis into consideration, an approximation for the associated displacement field within a plate-type domain can be given in the following form.

$$\left\{\tilde{u}^i, \tilde{v}^i, \tilde{w}_b^i, \tilde{w}_s^i\right\}^T = \sum_{i=1}^{m\times n} T_i(x, y)\begin{Bmatrix} u^i \\ v^i \\ w_b^i \\ w_s^i \end{Bmatrix}, \tag{24}$$

where,

$$T_i(x, y) = \begin{bmatrix} \mathfrak{J}_i(x, y) & 0 & 0 & 0 \\ 0 & \mathfrak{J}_i(x, y) & 0 & 0 \\ 0 & 0 & \mathfrak{J}_i(x, y) & 0 \\ 0 & 0 & 0 & \mathfrak{J}_i(x, y) \end{bmatrix}. \tag{25}$$

In accordance with Eq. (7), and considering Eq. (24), the strain components can be rewritten as below

$$\mathfrak{P}_b = \mathfrak{P}_b^L + \mathfrak{P}_b^{NL} = \sum_{i=1}^{m\times n} \mathcal{T}_{Lb}^i \mathbb{X} + \sum_{i=1}^{m\times n} \frac{1}{2}\mathcal{T}_{NLb}^i \mathbb{X}, \quad \mathfrak{P}_s = \sum_{i=1}^{m\times n} \mathcal{T}_s^i \mathbb{X}, \tag{26}$$

where

$$\begin{gathered}
\mathcal{T}_{Lb}^i = \left\{ \mathcal{T}_{b1}^i \ \mathcal{T}_{b2}^i \ \mathcal{T}_{b3}^i \ \mathcal{T}_{b4}^i \right\}^T, \quad \mathcal{T}_{NLb}^i = \left\{ \mathcal{T}_{b5}^i \ 0 \ 0 \ 0 \right\}^T \mathcal{T}_G^i, \quad \mathbb{X} = \begin{Bmatrix} u^i \\ v^i \\ w_b^i \\ w_s^i \end{Bmatrix}, \\
\mathcal{T}_{b1}^i = \begin{bmatrix} \mathfrak{J}_{i,x}(x, y) & 0 & 0 & 0 \\ 0 & \mathfrak{J}_{i,y}(x, y) & 0 & 0 \\ \mathfrak{J}_{i,y}(x, y) & \mathfrak{J}_{i,x}(x, y) & 0 & 0 \\ 0 & 0 & 0 & 0 \end{bmatrix}, \quad \mathcal{T}_{b2}^i = -\begin{bmatrix} 0 & 0 & \mathfrak{J}_{i,xx}(x, y) & 0 \\ 0 & 0 & \mathfrak{J}_{i,yy}(x, y) & 0 \\ 0 & 0 & 2\mathfrak{J}_{i,xy}(x, y) & 0 \\ 0 & 0 & 0 & 0 \end{bmatrix}, \\
\mathcal{T}_{b3}^i = \begin{bmatrix} 0 & 0 & 0 & \mathfrak{J}_{i,xx}(x, y) \\ 0 & 0 & 0 & \mathfrak{J}_{i,yy}(x, y) \\ 0 & 0 & 0 & 2\mathfrak{J}_{i,xy}(x, y) \\ 0 & 0 & 0 & 0 \end{bmatrix}, \quad \mathcal{T}_{b4}^i = \begin{bmatrix} 0 & 0 & 0 & 0 \\ 0 & 0 & 0 & 0 \\ 0 & 0 & 0 & 0 \\ 0 & 0 & 0 & \mathfrak{J}_i(x, y) \end{bmatrix}, \\
\mathcal{T}_{b5}^i = \begin{bmatrix} \frac{\partial w_b}{\partial x} + \frac{\partial w_s}{\partial x} & 0 \\ 0 & \frac{\partial w_b}{\partial y} + \frac{\partial w_s}{\partial y} \\ \frac{\partial w_b}{\partial y} + \frac{\partial w_s}{\partial y} & \frac{\partial w_b}{\partial x} + \frac{\partial w_s}{\partial x} \end{bmatrix}, \quad \mathcal{T}_G^i = \begin{bmatrix} 0 & 0 & \mathfrak{J}_{i,x}(x, y) & \mathfrak{J}_{i,x}(x, y) \\ 0 & 0 & \mathfrak{J}_{i,y}(x, y) & \mathfrak{J}_{i,y}(x, y) \end{bmatrix}
\end{gathered} \tag{27}$$

As a result, the variation of the strain tensor can be expressed as

$$\delta\left(\mathfrak{P}_b\right)=\delta\left(\mathfrak{P}_b^L\right)+\delta\left(\mathfrak{P}_b^{NL}\right)=\sum_{i=1}^{m\times n}\left(\mathcal{T}_{Lb}^{i}+\mathcal{T}_{NLb}^{i}\right)\begin{Bmatrix}\delta u^i\\ \delta v^i\\ \delta w_b^i\\ \delta w_s^i\end{Bmatrix},\quad \delta\left(\mathfrak{P}_s\right)=\sum_{i=1}^{m\times n}\mathcal{T}_s^{i}\begin{Bmatrix}\delta u^i\\ \delta v^i\\ \delta w_b^i\\ \delta w_s^i\end{Bmatrix}. \tag{28}$$

After that, the discretized form of the nonlinear differential equations of the system can be presented as follows

$$\mathfrak{T}(\mathbb{X})\mathbb{X}=\mathbb{p}, \tag{29}$$

where $\mathfrak{T}(\mathbb{X})$ stands for the global stiffness matrix including linear and nonlinear parts as below

$$\mathfrak{T}_L=\int_S\left\{\left(\mathcal{T}_{Lb}^{i}\right)^T\xi_b\mathcal{T}_{Lb}^{i}-l^2\nabla^2\left(\mathcal{T}_{Lb}^{i}\right)^T\xi_b\mathcal{T}_{Lb}^{i}+\left(\mathcal{T}_{s}^{i}\right)^T\xi_s\mathcal{T}_{s}^{i}-l^2\nabla^2\left(\mathcal{T}_{s}^{i}\right)^T\xi_s\mathcal{T}_{s}^{i}\right\}\mathrm{d}S, \tag{30a}$$

$$\begin{aligned}\mathfrak{T}_{NL}(\mathbb{X})=\int_S&\left\{\frac{1}{2}\left(\mathcal{T}_{Lb}^{i}\right)^T\xi_b\mathcal{T}_{NLb}^{i}-\frac{l^2}{2}\nabla^2\left(\mathcal{T}_{Lb}^{i}\right)^T\xi_b\mathcal{T}_{NLb}^{i}+\left(\mathcal{T}_{NLb}^{i}\right)^T\xi_b\mathcal{T}_{Lb}^{i}\right.\\&\left.-l^2\nabla^2\left(\mathcal{T}_{NLb}^{i}\right)^T\xi_b\mathcal{T}_{Lb}^{i}+\frac{1}{2}\left(\mathcal{T}_{NLb}^{i}\right)^T\xi_b\mathcal{T}_{NLb}^{i}-\frac{l^2}{2}\nabla^2\left(\mathcal{T}_{NLb}^{i}\right)^T\xi_b\mathcal{T}_{NLb}^{i}\right\}\mathrm{d}S\end{aligned} \tag{30b}$$

Also, the load vector can be given as

$$\mathbb{p}=\int_S\left(1-e^2\nabla^2\right)\begin{Bmatrix}0\\0\\ \mathfrak{J}_i(x,y)\\ \mathfrak{J}_i(x,y)\end{Bmatrix}\mathrm{d}S. \tag{31}$$

Thereafter, an iterative solution methodology based on the Newton–Raphson technique is employed to solve Eq. (29). To this purpose, the residual force vector is introduced as follows

$$\mathcal{R}(\mathbb{X})=\mathfrak{T}(\mathbb{X})\mathbb{X}-\mathbb{p}=\left[\mathfrak{T}_L+\mathfrak{T}_{NL}(\mathbb{X})\right]\mathbb{X}-\mathbb{p}. \tag{32}$$

Accordingly, the considered increment in the value of displacement vector is as below

$$\mathbb{X}=-\frac{\mathcal{R}\left(\mathbb{X}^i\right)}{\mathfrak{T}_L+\mathfrak{T}_{NL}+\mathfrak{T}_G}, \tag{33}$$

where

$$\mathbb{X}^{i+1}=\mathbb{X}^i+\mathbb{X}, \tag{34}$$

and $\mathfrak{T}_G$ is the geometric stiffness matrix which can be achieved in the following form

$$\mathfrak{T}_G=\int_S\left\{\left(\mathcal{T}_{G1}\right)^T\boldsymbol{N}_x\mathcal{T}_{G1}-l^2\nabla^2\left(\mathcal{T}_{G1}\right)^T\boldsymbol{N}_x\mathcal{T}_{G1}+\left(\mathcal{T}_{G2}\right)^T\boldsymbol{N}_y\mathcal{T}_{G2}-l^2\nabla^2\left(\mathcal{T}_{G2}\right)^T\boldsymbol{N}_y\mathcal{T}_{G2}\right\}\mathrm{d}S, \tag{35}$$

in which

$$\mathcal{T}_{G1}=\begin{bmatrix}0&0&\mathfrak{J}_{i,x}(x,y)&0\\0&0&\mathfrak{J}_{i,y}(x,y)&0\end{bmatrix},\quad \mathcal{T}_{G2}=\begin{bmatrix}0&0&0&\mathfrak{J}_{i,x}(x,y)\\0&0&0&\mathfrak{J}_{i,y}(x,y)\end{bmatrix}, \tag{36}$$

and $\boldsymbol{N}_x$, $\boldsymbol{N}_y$ are the load-type stress resultants along x axis and y axis, respectively.

4 Numerical results and discussion

The dimensionless nonlocal strain gradient load–deflection curves associated with the porosity-dependent nonlinear flexural response of the uniformly distributed loaded porous FGM microplates with and without a central cutout having different shapes are presented. It is assumed that the top and bottom surfaces of porous FGM microplates are ceramic-rich and metal-rich, respectively. The material properties are: $E_c=210$ GPa, $\nu=0.24$ for the ceramic phase, $E_m=70$ GPa, $\nu=0.35$ for the metal phase [89]. Also, the dimensionless load and deflection are calculated as $\overline{P}=PL_1^2/E_mh^3$,

$W = w/h$. Moreover, the geometric parameters are assumed as $h = 20$ μm, $L_1 = 50$ h, $L_1/L_2 = 1$.

At first, the validity of the present solution process is checked. To this end, by neglecting the size dependent terms, the nonlinear load–deflection response associated with the geometrically nonlinear flexural response of a square composite plate is obtained and compared with that presented by Singh et al. [90] as shown in Fig. 7. A very good can be observed which confirms the introduced numerical solution methodology.

In Figs. 8 and 9, the classical and nonlocal strain gradient load–deflection curves associated with the nonlinear bending response of U-PFGM microplates without any central cutout are displayed for various values of the nonlocal parameter and strain gradient parameter, respectively. By comparing the nonlocal strain gradient curves with the classical counterparts, it is deduced that by taking the strain gradient type of size dependency into consideration, the maximum deflection associated with a given applied distributed load gets smaller which indicated the stiffening influence of the couple stress size effect. However, in the presence of the nonlocal size effect, an opposite pattern is found which represents the softening influence of it. This observation has a similar pattern for the both fully simply supported (SSSS) and fully clamped (CCCC) boundary conditions.

Figures 10 and 11 illustrate the classical and nonlocal strain gradient load–deflection curves relevant to the

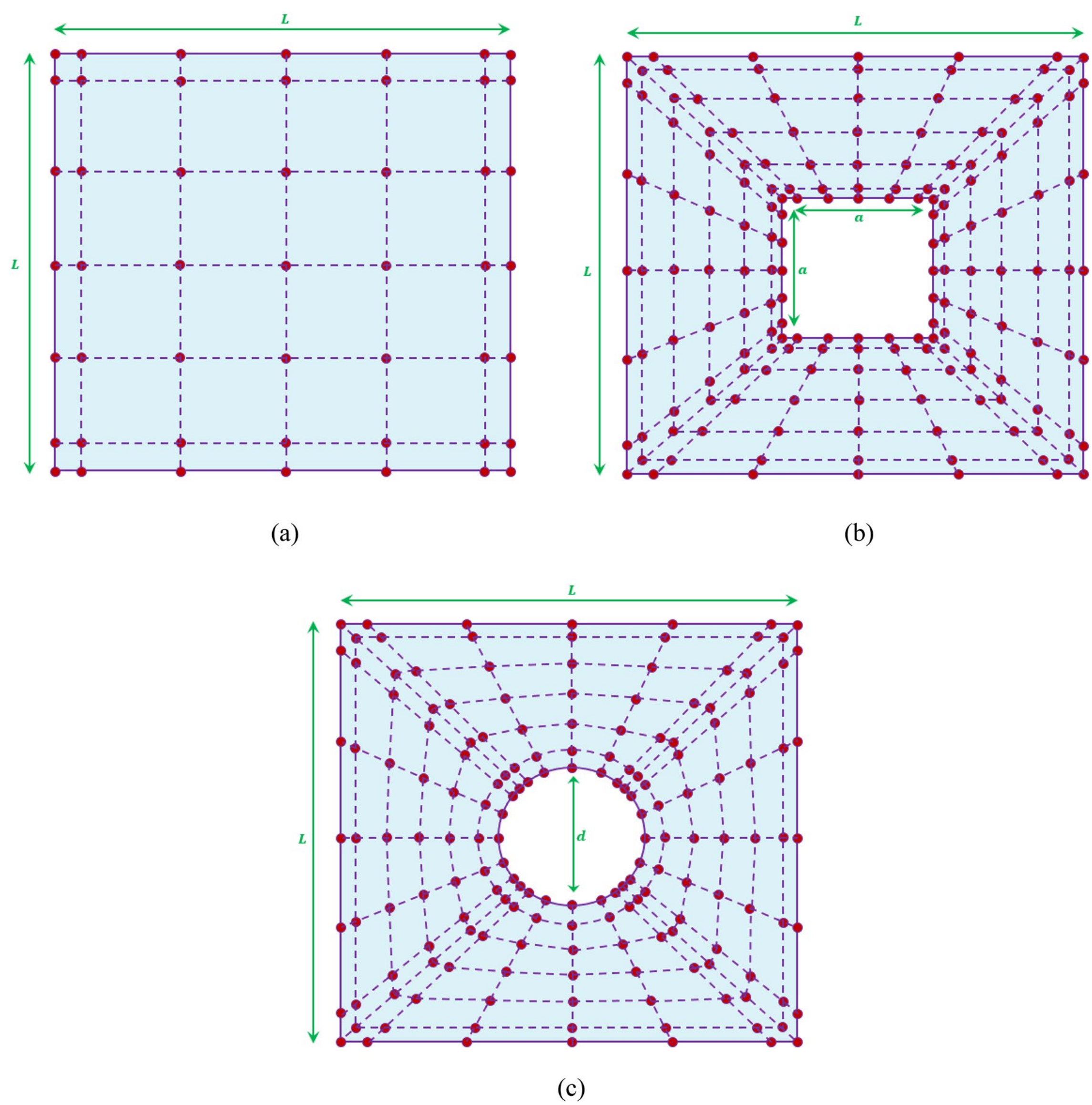

Fig. 6 Illustration of cubic elements for square microplates with geometrical parameters: **a** microplate without a central cutout, **b** microplate with a square cutout, **c** microplate with a circular cutout

nonlinear bending behavior of U-PFGM microplates without any central cutout corresponding to different material property gradient indexes, and respectively, for various nonlocal and strain gradient parameters. It is demonstrated that by moving from the fully ceramic-rich microplate to the fully metal-rich one, the rate of load–deflection variation decreases significantly, so a specific maximum deflection occurs at a lower applied distributed load. Also, the gap between the nonlocal strain gradient curve and its classical counterpart becomes larger by moving from the fully metal-rich microplate to the fully ceramic-rich one.

The classical and nonlocal strain gradient load–deflection curves associated with the nonlinear bending characteristics of porous FGM microplates without a central cutout are depicted in Figs. 12 and 13 corresponding to different porosity dispersion patterns. It is seen that by taking only the nonlocality into consideration, the gap between nonlinear bending curves relevant to various patterns of porosity dispersion is a bit lower for the nonlocal strain gradient case than the classical one. But, in the presence strain gradient size dependency and in the absence of nonlocality, the observation becomes reverse. In addition, a same trend can be observed for different patterns of porosity dispersion, and this issue is for the both types of SSSS and CCCC boundary conditions.

In Tables 1 and 2, the classical and nonlocal strain gradient dimensionless distributed loads associated with given maximum deflections resulted from the nonlinear bending response of porous FGM microplates without any central cutout are tabulated corresponding to different material property gradient indexes and in the presence and absence of one of the nonlocal and strain gradient size dependencies. The percentages presented in parentheses indicate the difference between the nonlocal strain gradient distributed load and its classical counterpart. It is revealed that for a larger maximum deflection, the significance of the both nonlocal and strain gradient reduces. This prediction is the same for all values of the material property gradient index. Furthermore, it can be seen that corresponding to different maximum deflections, the both nonlocality and strain gradient size effects on the distributed load is a bit lower for a fully clamped porous FGM microplate than that a fully simply supported one. It is revealed that among various patterns of porosity dispersion, the geometrically nonlinear bending stiffness associated with the O-PFGM and X-PFGM microplates is minimum and maximum, respectively.

In Fig. 14, the nonlocal strain gradient nonlinear bending responses of O-PFGM and X-PFGM microplates without any central cutout are shown corresponding to various values of the porosity index. It is obvious that for a porous FGM microplate with a higher value of the porosity index, the gap between nonlocal strain gradient nonlinear bending curves associated with the O-PFGM and X-PFGM dispersion patterns enhances. This anticipation may be related to this fact that a higher porosity index results in bigger internal pores that makes increase the importance of the role of porosity dispersion pattern. This conclusion can be deduced for the both types of SSSS and CCCC edge supports.

Tables 3 and 4 give the classical and nonlocal strain gradient dimensionless distributed loads associated with given maximum deflections resulted from the nonlinear bending response of porous FGM microplates without any central cutout corresponding to different porosity indexes and in the presence and absence of one of the nonlocal and strain gradient size dependencies. The percentages presented in parentheses indicate the difference between the nonlocal strain gradient distributed load and its classical counterpart. It is observed that corresponding to different maximum deflections, the significance of the strain gradient size effect in the absence of nonlocality on the nonlinear flexural stiffness of a porous FGM microplate is more than that of the nonlocal size effect in the absence of the strain gradient size dependency.

To indicate the influence of a central cutout with different shapes on the nonlocal strain gradient nonlinear bending characteristics of porous FGM microplates, the nonlinear load–deflection curves associated with U-PFGM microplates with square and circular shapes having various side lengths and diameters are plotted in Figs. 15 and 16, respectively. It can be found that a central cutout leads to change the trend of load–deflection response. As a consequence, for smaller value of the applied distributed load, the induced maximum deflection for a microplate without any central cutout is higher than that induced in microplates with a

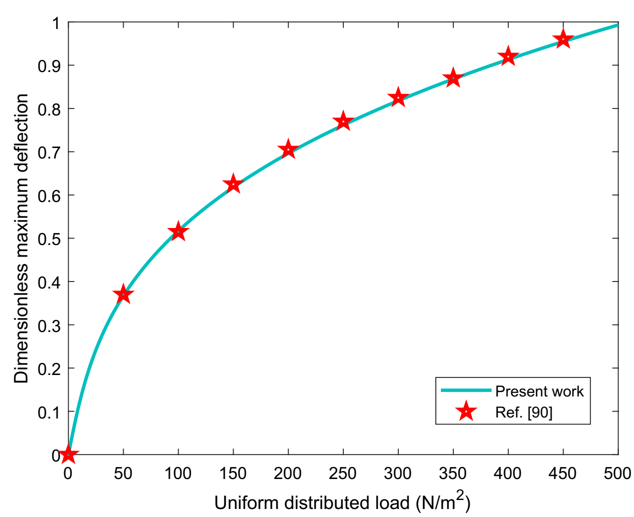

Fig. 7 Comparison of load deflection curves associated with the nonlinear bending of composite square plate under inform distributed load

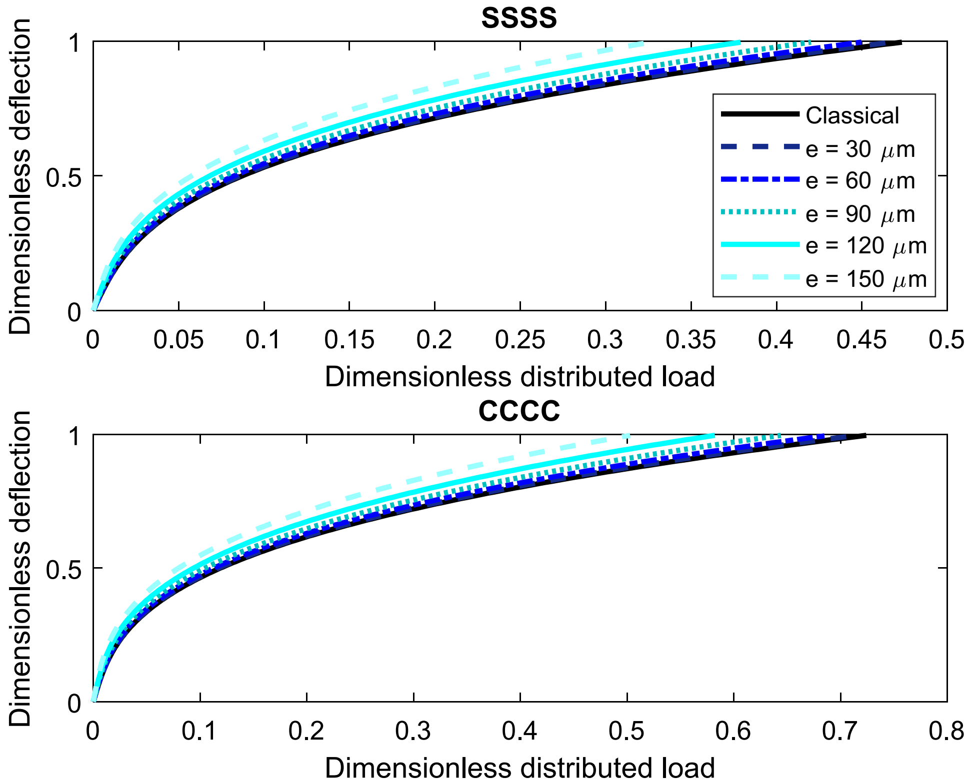

Fig. 8 Dimensionless classical and nonlocal strain gradient load–deflection responses associated with the nonlinear bending of U-PFGM microplates corresponding to various values of the nonlocal parameter in the absence of strain gradient size effect ($l = 0$ μm, $\Gamma = 0.4$, $k = 0.5$, $a/L = d/L = 0$)

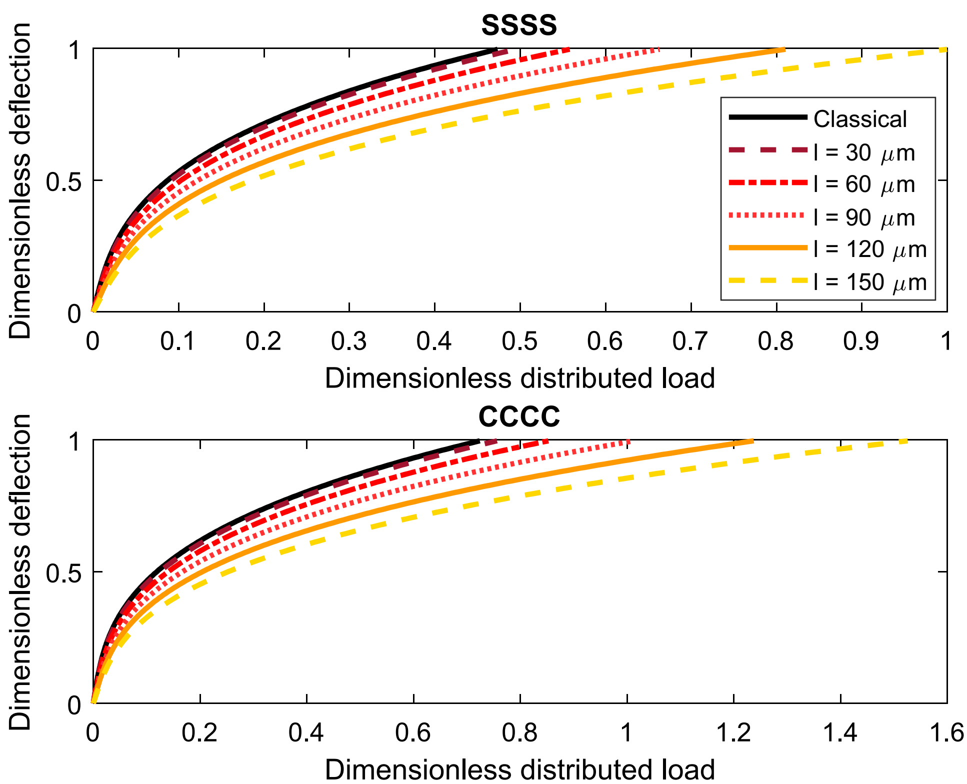

Fig. 9 Dimensionless classical and nonlocal strain gradient load–deflection responses associated with the nonlinear bending of U-PFGM microplates corresponding to various values of the strain gradient parameter in the absence of nonlocal size effect ($e = 0$ μm, $\Gamma = 0.4$, $k = 0.5$, $a/L = d/L = 0$)

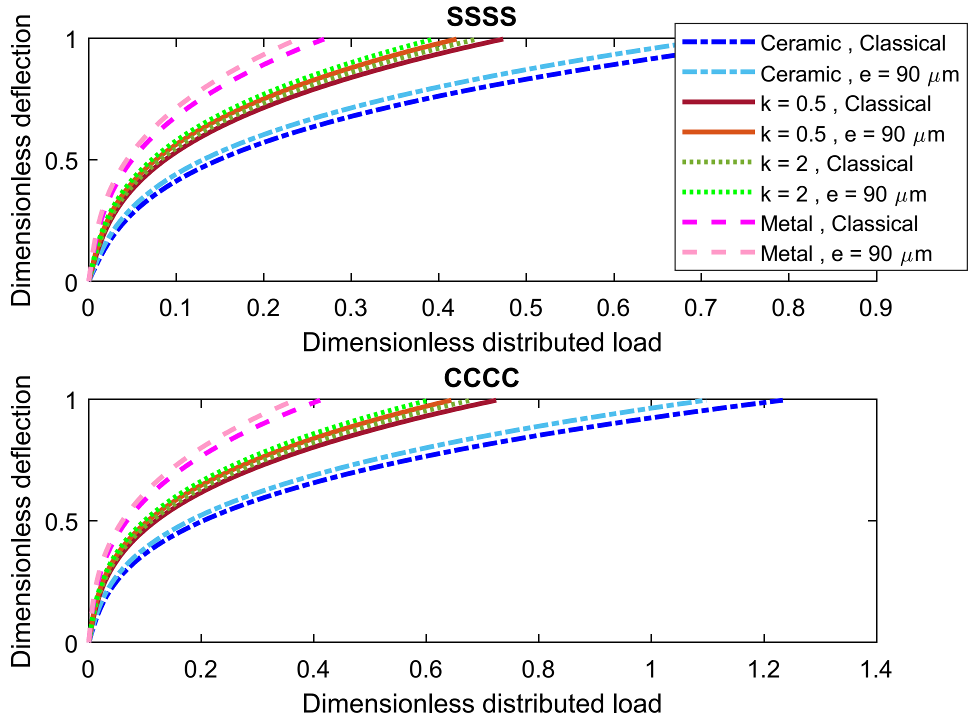

Fig. 10 Dimensionless classical and nonlocal strain gradient load–deflection responses associated with the nonlinear bending of U-PFGM microplates corresponding to various values of the material gradient index in the absence of strain gradient size dependency ($l = 0$ µm, $\Gamma = 0.4$, $a/L = d/L = 0$)

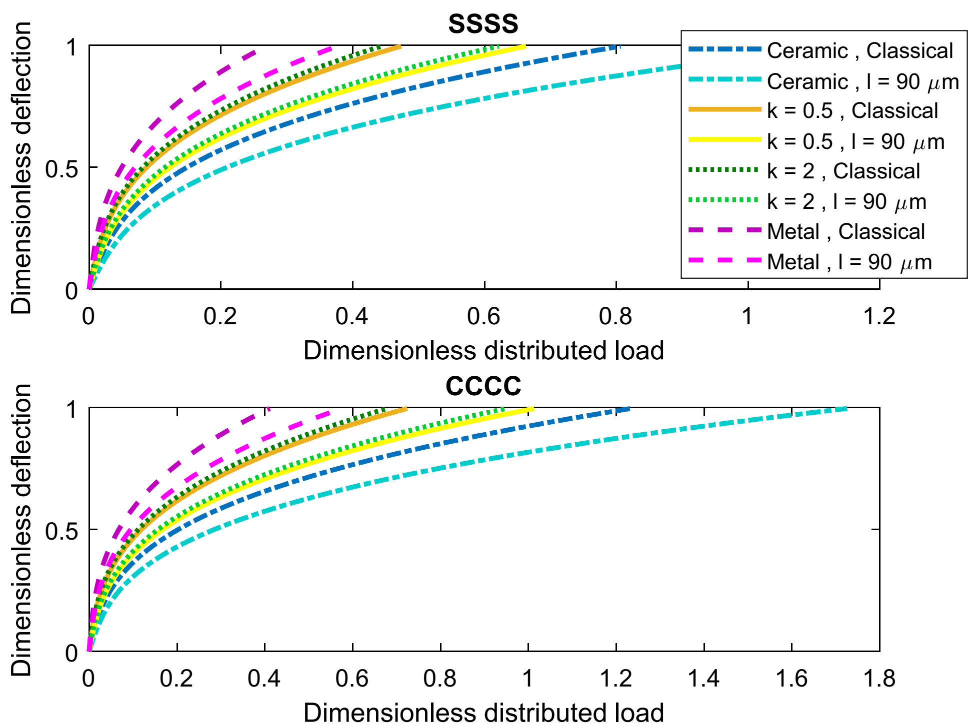

Fig. 11 Dimensionless classical and nonlocal strain gradient load–deflection responses associated with the nonlinear bending of U-PFGM microplates corresponding to various values of the material gradient index in the absence of nonlocal size dependency ($e = 0$ µm, $\Gamma = 0.4$, $a/L = d/L = 0$)

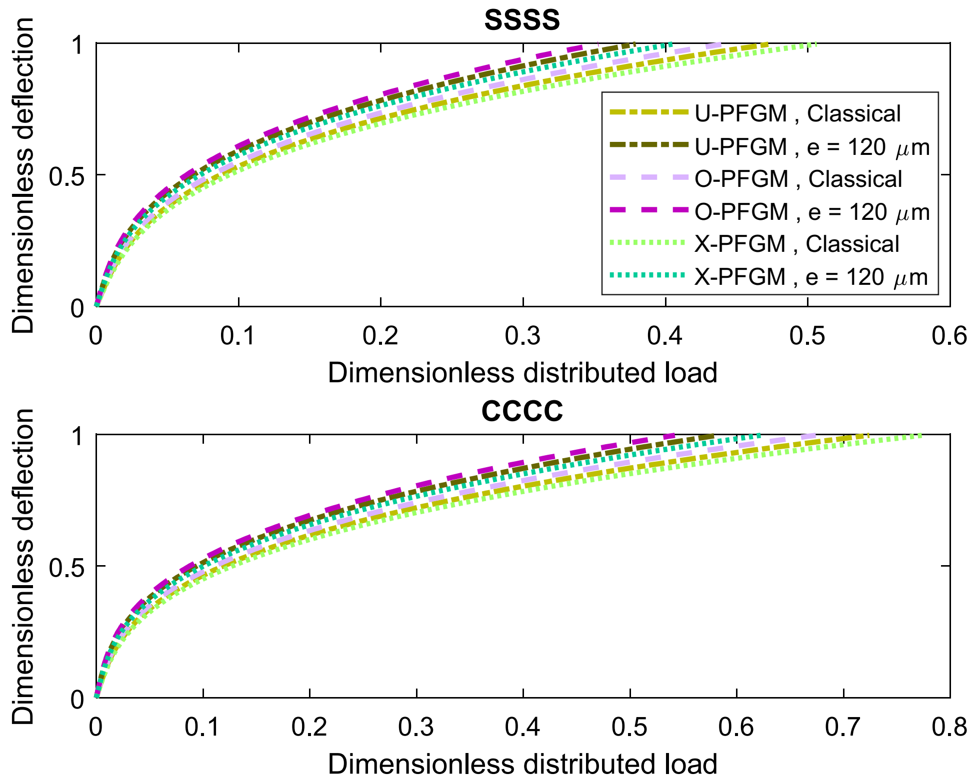

Fig. 12 Dimensionless classical and nonlocal strain gradient load–deflection responses associated with the nonlinear bending of porous FGM microplates corresponding to various porosity dispersion patterns in the absence of strain gradient size dependency ($l = 0$ μm, $\Gamma = 0.4$, $k = 0.5$, $a/L = d/L = 0$)

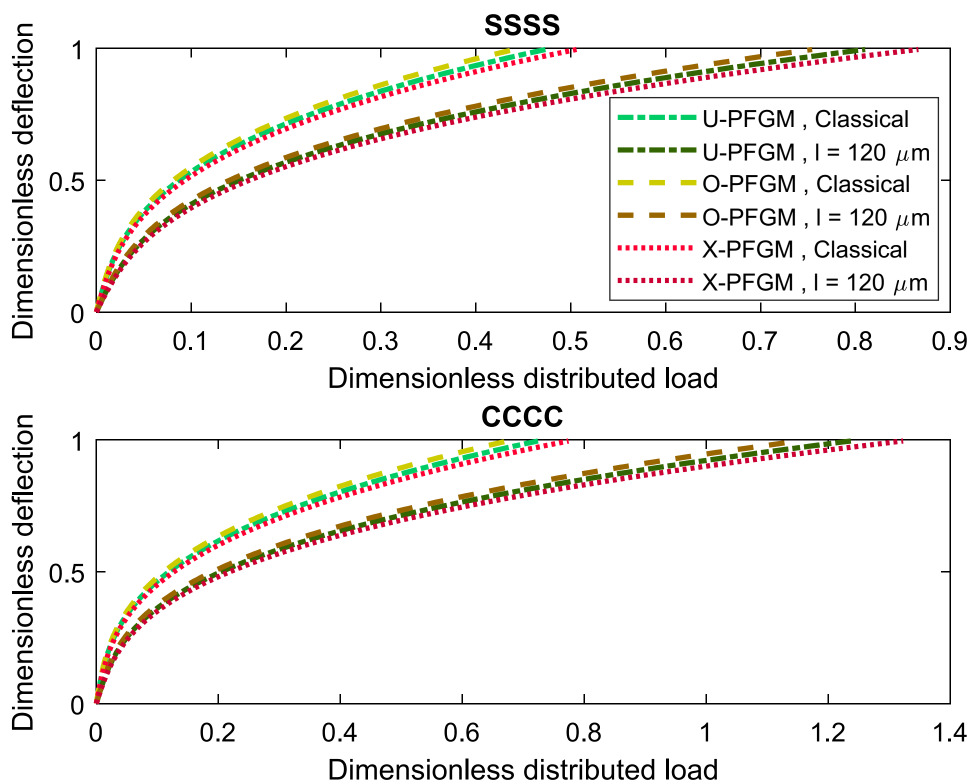

Fig. 13 Dimensionless classical and nonlocal strain gradient load–deflection responses associated with the nonlinear bending of porous FGM microplates corresponding to various porosity dispersion patterns in the absence of nonlocal size dependency ($e = 0$ μm, $\Gamma = 0.4$, $k = 0.5$, $a/L = d/L = 0$)

Table 1 Classical and nonlocal strain gradient dimensionless distributed loads of porous FG composite microplates corresponding to different nonlocal parameters, porosity dispersion patterns, maximum deflections, and various material property gradient indexes (Γ = 0.4, l = 0 μm)

k	e (μm)	U-PFGM	O-PFGM	X-PFGM
SSSS boundary conditions				
0.5	w/h = 0.4			
	0	0.0553	0.0515	0.0591
	60	0.0522 (−5.64%)	0.0486 (−5.64%)	0.0558 (−5.64%)
	120	0.0428 (−22.56%)	0.0399 (−22.55%)	0.0458 (−22.55%)
	w/h = 0.8			
	0	0.2662	0.2478	0.2846
	60	0.2526 (−5.11%)	0.2351 (−5.11%)	0.2700 (−5.11%)
	120	0.2118 (−20.41%)	0.1972 (−20.41%)	0.2265 (−20.41%)
2	w/h = 0.4			
	0	0.0518	0.0483	0.0554
	60	0.0489 (−5.64%)	0.0455 (−5.64%)	0.0523 (−5.64%)
	120	0.0402 (−22.56%)	0.0374 (−22.55%)	0.0429 (−22.56%)
	w/h = 0.8			
	0	0.2496	0.2324	0.2669
	60	0.2369 (−5.11%)	0.2205 (−5.11%)	0.2532 (−5.11%)
	120	0.1987 (−20.41%)	0.1849 (−20.41%)	0.2124 (−20.41%)
CCCC boundary conditions				
0.5	w/h = 0.4			
	0	0.0715	0.0666	0.0765
	60	0.0676 (−5.44%)	0.0630 (−5.44%)	0.0723 (−5.44%)
	120	0.0560 (−21.72%)	0.0521 (−21.72%)	0.0599 (−21.72%)
	w/h = 0.8			
	0	0.3961	0.3687	0.4234
	60	0.3763 (−4.98%)	0.3503 (−4.98%)	0.4023 (−4.98%)
	120	0.3172 (−19.92%)	0.2953 (−19.92%)	0.3391 (−19.92%)
2	w/h = 0.4			
	0	0.0671	0.0624	0.0717
	60	0.0634 (−5.44%)	0.0590 (−5.44%)	0.0678 (−5.44%)
	120	0.0525 (−21.72%)	0.0489 (21.72%)	0.0561 (−21.72%)
	w/h = 0.8			
	0	0.3714	0.3458	0.3971
	60	0.3529 (−4.98%)	0.3285 (−4.98%)	0.3773 (−4.98%)
	120	0.2975 (−19.92%)	0.2769 (−19.92%)	0.3180 (−19.92%)

central cutout. However, by increasing the distributed load, this pattern becomes vice versa. Accordingly, there is a specific value for the applied distributed load that this shift of

Table 2 Classical and nonlocal strain gradient dimensionless distributed loads of porous FG composite microplates corresponding to different strain gradient parameters, porosity dispersion patterns, maximum deflections, and various material property gradient indexes (Γ = 0.4, e = 0 μm)

k	l (μm)	U-PFGM	O-PFGM	X-PFGM
SSSS boundary conditions				
0.5	w/h = 0.4			
	0	0.0553	0.0515	0.0591
	60	0.0654 (+18.32%)	0.0609 (+18.32%)	0.0699 (+18.32%)
	120	0.0958 (+73.23%)	0.0892 (+73.23%)	0.1024 (+73.23%)
	w/h = 0.8			
	0	0.2662	0.2478	0.2846
	60	0.3139 (+17.91%)	0.2922 (+17.91%)	0.3355 (+17.91%)
	120	0.4566 (+71.53%)	0.4250 (+71.53%)	0.4881 (+71.53%)
2	w/h = 0.4			
	0	0.0518	0.0483	0.0554
	60	0.0613 (+18.32%)	0.0571 (+18.32%)	0.0656 (+18.32%)
	120	0.0898 (+73.23%)	0.0836 (+73.23%)	0.0960 (+73.23%)
	w/h = 0.8			
	0	0.2496	0.2324	0.2669
	60	0.2943 (+17.91%)	0.2740 (+17.91%)	0.3147 (+17.91%)
	120	0.4282 (+71.53%)	0.3986 (+71.53%)	0.4578 (+71.53%)
CCCC boundary conditions				
0.5	w/h = 0.4			
	0	0.0715	0.0666	0.0765
	60	0.0845 (+18.16%)	0.0787 (+18.16%)	0.0904 (+18.16%)
	120	0.1234 (+72.57%)	0.1149 (+72.57%)	0.1320 (+72.57%)
	w/h = 0.8			
	0	0.3961	0.3687	0.4234
	60	0.4666 (+17.82%)	0.4344 (+17.82%)	0.4989 (+17.82%)
	120	0.6778 (+71.14%)	0.6310 (+71.14%)	0.7246 (+71.14%)
2	w/h = 0.4			
	0	0.0671	0.0624	0.0717
	60	0.0793 (+18.16%)	0.0738 (+18.16%)	0.0847 (+18.16%)
	120	0.1158 (+72.57%)	0.1078 (+72.57%)	0.1238 (+72.57%)
	w/h = 0.8			
	0	0.3714	0.3458	0.3971
	60	0.4376 (+17.82%)	0.4074 (+17.82%)	0.4678 (+17.82%)
	120	0.6357 (+71.14%)	0.5917 (+71.14%)	0.6796 (+71.14%)

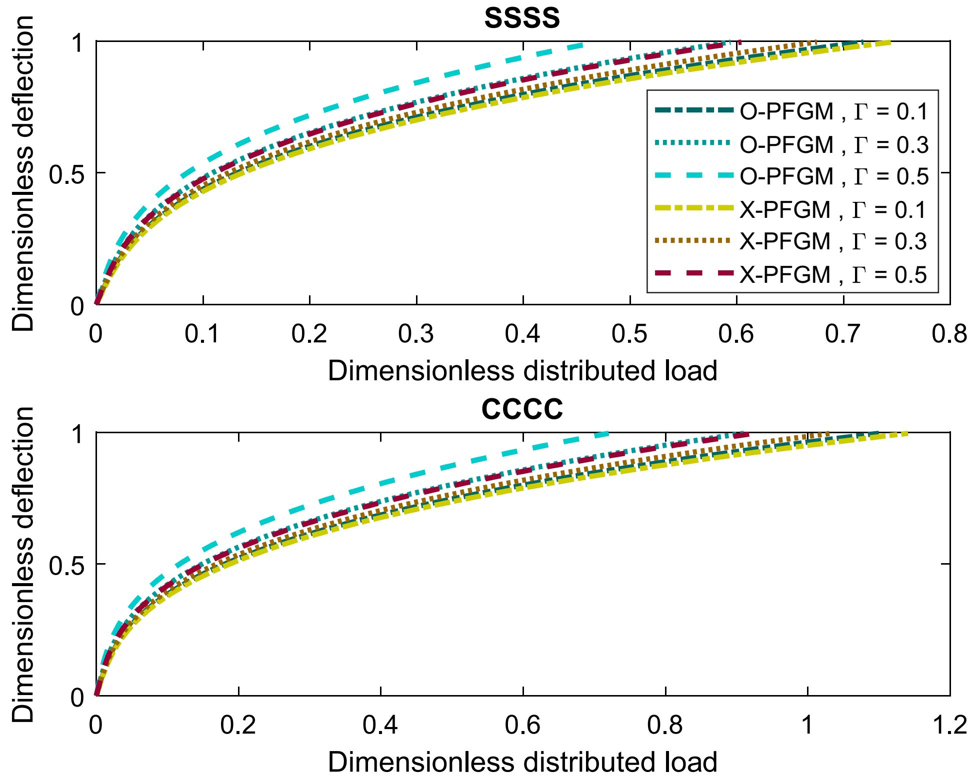

Fig. 14 Dimensionless nonlocal strain gradient load–deflection responses associated with the nonlinear bending of porous FGM microplates corresponding to various values of the porosity index ($e = l = 120$ µm, $k = 0.5$, $a/L = d/L = 0$)

trend occurs, and it depends on several parameters such as the cutout geometry and boundary conditions.

5 Conclusion

In this work, the nonlocal strain gradient geometrically nonlinear flexural response of porous FGM microplates having a central cutout with different shapes was predicted. To accomplish this issue, a hybrid-type quasi-3D higher-order shear deformation plate theory was formulated within the framework of the nonlocal strain gradient continuum elasticity. Afterwards, using the NURBS-based isogeometric approach, the possibility of flexibly meeting higher-order derivatives was achieved.

It was indicated that by taking the strain gradient type of size dependency into consideration, the maximum deflection associated with a given applied distributed load gets smaller which indicated the stiffening influence of the couple stress size effect. However, in the presence of the nonlocal size effect, an opposite pattern is found which represents the softening influence of it. Also, the gap between the nonlocal strain gradient curve and its classical counterpart becomes larger by moving from the fully metal-rich microplate to the fully ceramic-rich one. Additionally, it was found that for a larger maximum deflection, the significance of the both nonlocal and strain gradient reduces. This prediction was the same for all values of the material property gradient index as well as porosity index.

Furthermore, it was seen that corresponding to different maximum deflections, the significance of the strain gradient size effect in the absence of nonlocality on the nonlinear flexural stiffness of a porous FGM microplate is more than that of the nonlocal size effect in the absence of the strain gradient size dependency. In addition, it was revealed that a central cutout leads to change the trend of load–deflection

Table 3 Classical and nonlocal strain gradient dimensionless distributed loads of porous FG composite microplates corresponding to different nonlocal parameters, porosity dispersion patterns, maximum deflections, and various porosity indexes (k = 0.5, l = 0 μm)

Γ	e (μm)	U-PFGM	O-PFGM	X-PFGM
SSSS boundary conditions				
0.3	w/h = 0.4			
	0	0.0587	0.0559	0.0616
	60	0.0554 (−5.64%)	0.0527 (−5.64%)	0.0581 (−5.64%)
	120	0.0455 (−22.56%)	0.0433 (−22.56%)	0.0477 (−22.56%)
	w/h = 0.8			
	0	0.2828	0.2690	0.2966
	60	0.2683 (−5.11%)	0.2553 (−5.11%)	0.2814 (−5.11%)
	120	0.2251 (−20.41%)	0.2141 (−20.41%)	0.2361 (−20.41%)
0.5	w/h = 0.4			
	0	0.0517	0.0470	0.0565
	60	0.0488 (−5.64%)	0.0443 (−5.64%)	0.0533 (−5.64%)
	120	0.0401 (−22.56%)	0.0364 (−22.56%)	0.0437 (−22.56%)
	w/h = 0.8			
	0	0.2490	0.2261	0.2720
	60	0.2363 (−5.11%)	0.2145 (−5.11%)	0.2581 (−5.11%)
	120	0.1982 (−20.41%)	0.1799 (−20.41%)	0.2165 (−20.41%)
CCCC boundary conditions				
0.3	w/h = 0.4			
	0	0.0760	0.0723	0.0797
	60	0.0719 (−5.44%)	0.0684 (−5.44%)	0.0754 (−5.44%)
	120	0.0595 (−21.72%)	0.0566 (−21.72%)	0.0624 (−21.72%)
	w/h = 0.8			
	0	0.4208	0.4003	0.4413
	60	0.3998 (−4.98%)	0.3803 (−4.98%)	0.4193 (−4.98%)
	120	0.3370 (−19.92%)	0.3206 (−19.92%)	0.3534 (−19.92%)
0.5	w/h = 0.4			
	0	0.0669	0.0608	0.0731
	60	0.0633 (−5.44%)	0.0574 (−5.44%)	0.0691 (−5.44%)
	120	0.0524 (−21.72%)	0.0476 (−21.72%)	0.0572 (−21.72%)
	w/h = 0.8			
	0	0.3706	0.3364	0.4047
	60	0.3521 (−4.98%)	0.3196 (−4.98%)	0.3845 (−4.98%)
	120	0.2968 (−19.92%)	0.2694 (−19.92%)	0.3241 (−19.92%)

response. As a consequence, for smaller value of the applied distributed load, the induced maximum deflection for a microplate without any central cutout is higher than that induced in microplates with a central cutout. However, by increasing the distributed load, this pattern becomes vice versa.

Table 4 Classical and nonlocal strain gradient dimensionless distributed loads of porous FG composite microplates corresponding to different strain gradient parameters, porosity dispersion patterns, maximum deflections, and various porosity indexes (k = 0.5, e = 0 μm)

Γ	l (μm)	U-PFGM	O-PFGM	X-PFGM
SSSS boundary conditions				
0.3	w/h = 0.4			
	0	0.0587	0.0559	0.0616
	60	0.0695 (+18.32%)	0.0661 (+18.32)	0.0729 (+18.32%)
	120	0.1018 (+73.23%)	0.0968 (+73.23%)	0.1067 (+73.23%)
	w/h = 0.8			
	0	0.2828	0.2690	0.2966
	60	0.3335 (+17.91%)	0.3172 (+17.91%)	0.3497 (+17.91%)
	120	0.4851 (+71.53%)	0.4615 (+71.53%)	0.5088 (+71.53%)
0.5	w/h = 0.4			
	0	0.0517	0.0470	0.0565
	60	0.0612 (+18.32%)	0.0556 (+18.32%)	0.0668 (+18.32%)
	120	0.0896 (+73.23%)	0.0814 (+73.23%)	0.0979 (+73.23%)
	w/h = 0.8			
	0	0.2490	0.2261	0.2720
	60	0.2936 (+17.91%)	0.2666 (+17.91%)	0.3207 (+17.91%)
	120	0.4272 (+71.53%)	0.3878 (+71.53%)	0.4666 (+71.53%)
CCCC boundary conditions				
0.3	w/h = 0.4			
	0	0.0760	0.0723	0.0797
	60	0.0898 (+18.16%)	0.0854 (+18.16%)	0.0942 (+18.16%)
	120	0.1311 (+72.57%)	0.1247 (+72.57%)	0.1375 (+72.57%)
	w/h = 0.8			
	0	0.4208	0.4003	0.4413
	60	0.4958 (+17.82%)	0.4716 (+17.82%)	0.5200 (+17.82%)
	120	0.7202 (+71.14%)	0.6850 (+71.14%)	0.7553 (+71.14%)
0.5	w/h = 0.4			
	0	0.0669	0.0608	0.0731
	60	0.0791 (+18.16%)	0.0718 (+18.16%)	0.0864 (+18.16%)
	120	0.1155 (+72.57%)	0.1048 (+72.57%)	0.1261 (+72.57%)
	w/h = 0.8			
	0	0.3706	0.3364	0.4047
	60	0.4366 (+17.82%)	0.3963 (+17.82%)	0.4768 (+17.82%)
	120	0.6342 (+71.14%)	0.5757 (+71.14%)	0.6926 (+71.14%)

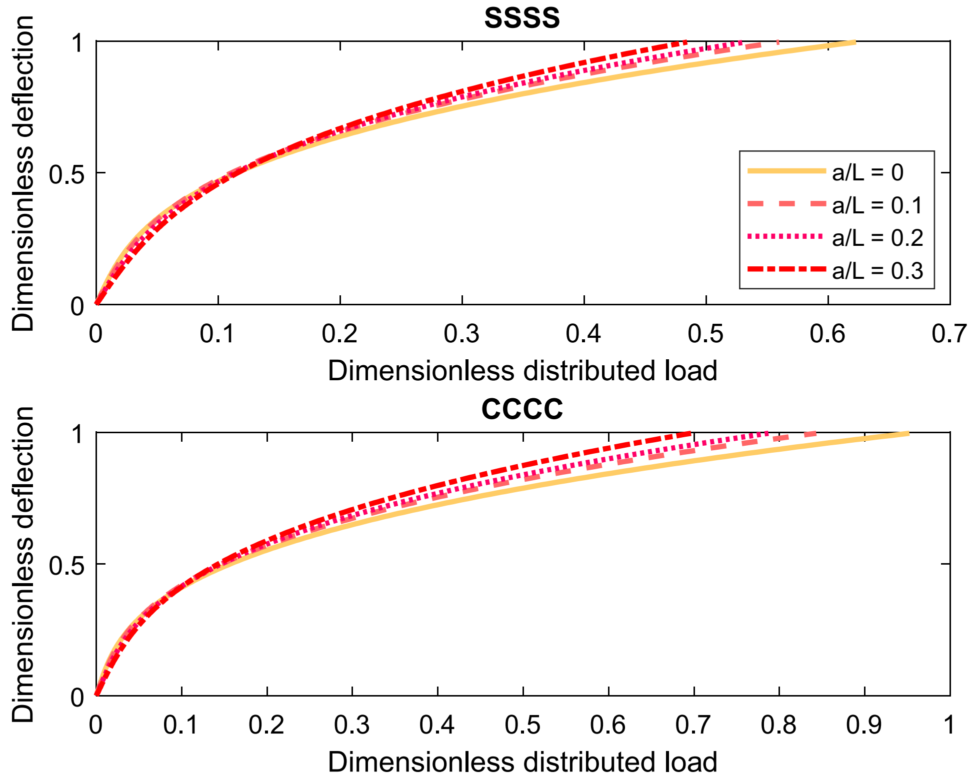

Fig. 15 Influence of a square central cutout on dimensionless nonlocal strain gradient load–deflection responses associated with the nonlinear bending of U-PFGM microplates ($e = l = 120$ μm, $\Gamma = 0.4$, $k = 0.5$)

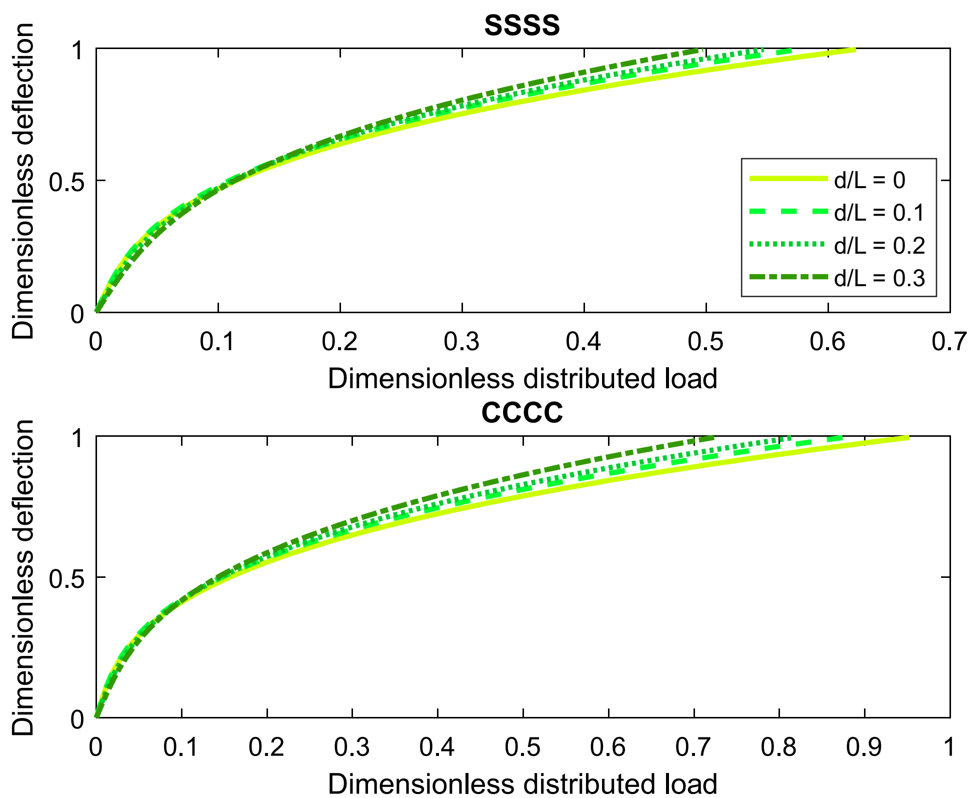

Fig. 16 Influence of a circular central cutout on dimensionless nonlocal strain gradient load–deflection responses associated with the nonlinear bending of U-PFGM microplates ($e = l = 120$ μm, $\Gamma = 0.4$, $k = 0.5$)

References

1. Cheng H, Li L, Wang B, Feng X, Mao Z, Vancso GJ, Sui X (2020) Multifaceted applications of cellulosic porous materials in environment, energy, and health. Prog Polym Sci 106:101253
2. Wang H, Liu X, Niu P, Wang S, Shi J, Li L (2020) Porous two-dimensional materials for photocatalytic and electrocatalytic applications. Matter 2:1377–1413
3. Guo H, Li X, Zhu Q, Zhang Z, Liu Y et al (2020) Imaging nano-defects of metal waveguides using the microwave cavity interference enhancement method. Nanotechnology 31:455203
4. Zhang W, Bao Y, Bao A (2020) Preparation of nitrogen-doped hierarchical porous carbon materials by a template-free method and application to CO_2 capture. J Environ Chem Eng 8:103732
5. Yu K, Wang J, Wang X, Liang J, Liang C (2020) Sustainable application of biomass by-products: Corn straw-derived porous carbon nanospheres using as anode materials for lithium ion batteries. Mater Chem Phys 243:122644
6. Safaei B (2020) The effect of embedding a porous core on the free vibration behavior of laminated composite plates. Steel Compos Struct 35:659–670
7. Gao W, Qin Z, Chu F (2020) Wave propagation in functionally graded porous plates reinforced with graphene platelets. Aerosp Sci Technol 102:105860
8. Moradi-Dastjerdi R, Behdinan K, Safaei B, Qin Z (2020) Static performance of agglomerated CNT-reinforced porous plates bonded with piezoceramic faces. Int J Mech Sci 188:105966
9. Lin J, Hu J, Wang W, Liu K, Zhou C et al (2021) Thermo and light-responsive strategies of smart titanium-containing composite material surface for enhancing bacterially anti-adhesive property. Chem Eng J 407:125783
10. Zhou Y, Zhu J (2016) Vibration and bending analysis of multiferroic rectangular plates using third-order shear deformation theory. Compos Struct 153:712–723
11. Sahmani S, Ansari R (2011) Nonlocal beam models for buckling of nanobeams using state-space method regarding different boundary conditions. J Mech Sci Technol 25:2365
12. Reddy JN, Romanoff J, Loya JA (2016) Nonlinear finite element analysis of functionally graded circular plates with modified couple stress theory. Eur J Mech A/Solids 56:92–104
13. Togun N, Bagdatli SM (2016) Size dependent nonlinear vibration of the tensioned nanobeam based on the modified couple stress theory. Compos B Eng 97:255–262
14. Sahmani S, Aghdam MM (2017) Axial postbuckling analysis of multilayer functionally graded composite nanoplates reinforced with GPLs based on nonlocal strain gradient theory. Eur Phys J Plus 132:1–17
15. Sahmani S, Aghdam MM, Bahrami M (2017) Surface free energy effects on the postbuckling behavior of cylindrical shear deformable nanoshells under combined axial and radial compressions. Meccanica 52:1329–1352
16. Joshi PV, Gupta A, Jain NK, Salhotra R, Rawani AM, Ramtekkar GD (2017) Effect of thermal environment on free vibration and buckling of partially cracked isotropic and FGM micro plates based on a non classical Kirchhoff's plate theory: an analytical approach. Int J Mech Sci 131:155–170
17. Malikan M (2017) Electro-mechanical shear buckling of piezoelectric nanoplate using modified couple stress theory based on simplified first order shear deformation theory. Appl Math Model 48:196–207
18. Sahmani S, Aghdam MM (2017) Size-dependent nonlinear bending of micro/nano-beams made of nanoporous biomaterials including a refined truncated cube cell. Phys Lett A 381:3818–3830
19. She G-L, Yuan F-G, Ren Y-R (2017) Nonlinear analysis of bending, thermal buckling and post-buckling for functionally graded tubes by using a refined beam theory. Compos Struct 165:74–82
20. Sahmani S, Fattahi AM (2018) Small scale effects on buckling and postbuckling behaviors of axially loaded FGM nanoshells based on nonlocal strain gradient elasticity theory. Appl Math Mech 39:561–580
21. Arefi M, Bidgoli EMR, Dimitri R, Tornabene F (2018) Free vibrations of functionally graded polymer composite nanoplates reinforced with graphene nanoplatelets. Aerosp Sci Technol 81:108–117
22. Sahmani S, Aghdam MM, Rabczuk T (2018) Nonlinear bending of functionally graded porous micro/nano-beams reinforced with graphene platelets based upon nonlocal strain gradient theory. Compos Struct 186:68–78
23. Sahmani S, Aghdam MM, Rabczuk T (2018) A unified nonlocal strain gradient plate model for nonlinear axial instability of functionally graded porous micro/nano-plates reinforced with graphene platelets. Mater Res Express 5:045048
24. Sahmani S, Aghdam MM, Rabczuk T (2018) Nonlocal strain gradient plate model for nonlinear large-amplitude vibrations of functionally graded porous micro/nano-plates reinforced with GPLs. Compos Struct 198:51–62
25. Fattahi AM, Safaei B, Ahmed NA (2019) A comparison for the non-classical plate model based on axial buckling of single-layered graphene sheets. Eur Phys J Plus 134:555
26. Safaei B, Khoda FH, Fattahi AM (2019) Non-classical plate model for single-layered graphene sheet for axial buckling. Adv Nano Res 7:265–275
27. Fattahi AM, Safaei B, Moaddab E (2019) The application of nonlocal elasticity to determine vibrational behavior of FG nanoplates. Steel Compos Struct 32:281–292
28. Sahmani S, Fattahi AM, Ahmed NA (2020) Analytical treatment on the nonlocal strain gradient vibrational response of postbuckled functionally graded porous micro-/nanoplates reinforced with GPL. Eng Comput 36:1559–1578
29. Li X, Li L, Hu Y, Ding Z, Deng W (2017) Sustainable application of biomass by-products: Corn straw-derived porous carbon nanospheres using as anode materials for lithium ion batteries. Compos Struct 165:250–265
30. Nguyen HX, Nguyen TN, Abdel-Wahab M, Bordas SPA et al (2017) A refined quasi-3D isogeometric analysis for functionally graded microplates based on the modified couple stress theory. Comput Methods Appl Mech Eng 313:904–940
31. Radic N, Jeremic D (2017) A comprehensive study on vibration and buckling of orthotropic double-layered graphene sheets under hygrothermal loading with different boundary conditions. Compos B Eng 128:182–199
32. Sahmani S, Aghdam MM (2017) Size dependency in axial postbuckling behavior of hybrid FGM exponential shear deformable nanoshells based on the nonlocal elasticity theory. Compos Struct 166:104–113
33. Sahmani S, Aghdam MM (2017) Temperature-dependent nonlocal instability of hybrid FGM exponential shear deformable nanoshells including imperfection sensitivity. Int J Mech Sci 122:129–142
34. Sahmani S, Aghdam MM (2017) Nonlinear instability of hydrostatic pressurized hybrid FGM exponential shear deformable nanoshells based on nonlocal continuum elasticity. Compos B Eng 114:404–417
35. Al-Shujairi M, Mollamahmutoglu C (2018) Buckling and free vibration analysis of functionally graded sandwich micro-beams resting on elastic foundation by using nonlocal strain gradient theory in conjunction with higher order shear theories under thermal effect. Compos B Eng 154:292–312

36. Jia XL, Ke LL, Zhong XL, Sun Y, Yang J, Kitipornchai S (2018) Thermal-mechanical-electrical buckling behavior of functionally graded micro-beams based on modified couple stress theory. Compos Struct 202:625–634
37. Thanh C-L, Phung-Van P, Thai CH, Nguyen-Xuan H, Abdel Wahab M (2018) Isogeometric analysis of functionally graded carbon nanotube reinforced composite nanoplates using modified couple stress theory. Compos Struct 184:633–649
38. Taati E (2018) On buckling and post-buckling behavior of functionally graded micro-beams in thermal environment. Int J Eng Sci 128:63–78
39. Hajmohammad MH, Zarei MS, Sepehr M, Abtahi N (2018) Bending and buckling analysis of functionally graded annular microplate integrated with piezoelectric layers based on layerwise theory using DQM. Aerosp Sci Technol 79:679–688
40. Soleimani I, Tadi Beni Y (2018) Vibration analysis of nanotubes based on two-node size dependent axisymmetric shell element. Arch Civil Mech Eng 18:1345–1358
41. Ghorbani Shenas A, Ziaee S, Malekzadeh P (2019) Post-buckling and vibration of post-buckled rotating pre-twisted FG microbeams in thermal environment. Thin Walled Struct 138:335–360
42. Sahmani S, Fattahi AM, Sahmani S (2020) Surface elastic shell model for nonlinear primary resonant dynamics of FG porous nanoshells incorporating modal interactions. Int J Mech Sci 165:105203
43. Sarafraz A, Sahmani S, Aghdam MM (2020) Nonlinear primary resonance analysis of nanoshells including vibrational mode interactions based on the surface elasticity theory. Appl Math Mech 41:233–260
44. Li Q, Xie B, Sahmani S, Safaei B (2020) Surface stress effect on the nonlinear free vibrations of functionally graded composite nanoshells in the presence of modal interaction. J Braz Soc Mech Sci Eng 42:237
45. Yi H, Sahmani S, Safaei B (2020) On size-dependent large-amplitude free oscillations of FGPM nanoshells incorporating vibrational mode interactions. Arch Civil Mech Eng 20:1–23
46. Sobhy M, Zenkour AM (2019) Porosity and inhomogeneity effects on the buckling and vibration of double-FGM nanoplates via a quasi-3D refined theory. Compos Struct 220:289–303
47. Phung-Van P, Thai CH, Nguyen-Xuan H, Abdel Wahab M (2019) Porosity-dependent nonlinear transient responses of functionally graded nanoplates using isogeometric analysis. Compos Part B Eng 164:215–225
48. Aria AI, Friswell MI (2019) Computational hygro-thermal vibration and buckling analysis of functionally graded sandwich microbeams. Compos B Eng 165:785–797
49. Yu YJ, Zhang K, Deng ZC (2019) Buckling analyses of three characteristic-lengths featured size-dependent gradient-beam with variational consistent higher order boundary conditions. Appl Math Model 74:1–20
50. Sahmani S, Safaei B (2019) Nonlinear free vibrations of bi-directional functionally graded micro/nano-beams including nonlocal stress and microstructural strain gradient size effects. Thin Walled Struct 140:342–356
51. Sahmani S, Safaei B (2019) Nonlocal strain gradient nonlinear resonance of bi-directional functionally graded composite micro/nano-beams under periodic soft excitation. Thin Walled Struct 143:106226
52. Sahmani S, Safaei B (2020) Influence of homogenization models on size-dependent nonlinear bending and postbuckling of bi-directional functionally graded micro/nano-beams. Appl Math Model 82:336–358
53. Thai CH, Ferreira AJM, Phung-Van P (2019) Size dependent free vibration analysis of multilayer functionally graded GPLRC microplates based on modified strain gradient theory. Compos B Eng 169:174–188
54. Thanh C-L, Tran LV, Vu-Huu T, Abdel-Wahab M (2019) The size-dependent thermal bending and buckling analyses of composite laminate microplate based on new modified couple stress theory and isogeometric analysis. Comput Methods Appl Mech Eng 350:337–361
55. Fang J, Zheng S, Xiao J, Zhang X (2020) Vibration and thermal buckling analysis of rotating nonlocal functionally graded nanobeams in thermal environment. Aerosp Sci Technol 106:106146
56. Yuan Y, Zhao K, Han Y, Sahmani S, Safaei B (2020) Nonlinear oscillations of composite conical microshells with in-plane heterogeneity based upon a couple stress-based shell model. Thin Walled Struct 154:106857
57. Yuan Y, Zhao K, Zhao Y, Sahmani S, Safaei B (2020) Couple stress-based nonlinear buckling analysis of hydrostatic pressurized functionally graded composite conical microshells. Mech Mater 148:103507
58. Yuan Y, Zhao X, Zhao Y, Sahmani S, Safaei B (2021) Dynamic stability of nonlocal strain gradient FGM truncated conical microshells integrated with magnetostrictive facesheets resting on a nonlinear viscoelastic foundation. Thin-Walled Structures 159:107249
59. Sarthak D, Prateek G, Vasudevan R, Polit O, Ganapathi M (2020) Dynamic buckling of classical/non-classical curved beams by nonlocal nonlinear finite element accounting for size dependent effect and using higher-order shear flexible model. Int J Non Linear Mech 125:103536
60. Thai CH, Tran TD, Phung-Van P (2020) A size-dependent moving Kriging meshfree model for deformation and free vibration analysis of functionally graded carbon nanotube-reinforced composite nanoplates. Eng Anal Bound Elem 115:52–63
61. Zhang B, Li H, Kong L, Shen H, Zhang Z (2020) Size-dependent static and dynamic analysis of Reddy-type micro-beams by strain gradient differential quadrature finite element method. Thin Walled Struct 148:106496
62. Sahmani S, Safaei B (2021) Large-amplitude oscillations of composite conical nanoshells with in-plane heterogeneity including surface stress effect. Appl Math Model 89:1792–1813
63. Fan F, Lei B, Sahmani S, Safaei B (2020) On the surface elastic-based shear buckling characteristics of functionally graded composite skew nanoplates. Thin Walled Struct 154:106841
64. Yuan Y, Zhao K, Sahmani S, Safaei B (2020) Size-dependent shear buckling response of FGM skew nanoplates modeled via different homogenization schemes. Appl Math Mech 41:587–604
65. Karamanli A, Vo TP (2020) Size-dependent behaviour of functionally graded sandwich microbeams based on the modified strain gradient theory. Compos Struct 246:112401
66. Fan L, Sahmani S, Safaei B (2020) Couple stress-based dynamic stability analysis of functionally graded composite truncated conical microshells with magnetostrictive facesheets embedded within nonlinear viscoelastic foundations. Eng Comput. https://doi.org/10.1007/s00366-020-01182-w
67. Guo J, Sun T, Pan E (2020) Three-dimensional nonlocal buckling of composite nanoplates with coated one-dimensional quasicrystal in an elastic medium. Int J Solids Struct 185:272–280
68. Ghane M, Saidi AR, Bahaadini R (2020) Vibration of fluid-conveying nanotubes subjected to magnetic field based on the thin-walled Timoshenko beam theory. Appl Math Model 80:65–83
69. Mao JJ, Lu HM, Zhang W, Lai SK (2020) Vibrations of graphene nanoplatelet reinforced functionally gradient piezoelectric composite microplate based on nonlocal theory. Compos Struct 236:111813
70. Thanh CL, Nguyen TN, Vu TH, Khatir S, Abdel Wahab M (2020) A geometrically nonlinear size-dependent hypothesis for porous functionally graded micro-plate. Eng Comput. https://doi.org/10.1007/s00366-020-01154-0

71. Fan F, Xu Y, Sahmani S, Safaei B (2020) Modified couple stress-based geometrically nonlinear oscillations of porous functionally graded microplates using NURBS-based isogeometric approach. Comput Methods Appl Mech Eng 372:113400
72. Fan F, Safaei B, Sahmani S (2021) Buckling and postbuckling response of nonlocal strain gradient porous functionally graded micro/nano-plates via NURBS-based isogeometric analysis. Thin-Walled Structures 159:107231.
73. Fan F, Sahmani S, Safaei B (2021) Isogeometric nonlinear oscillations of nonlocal strain gradient PFGM micro/nano-plates via NURBS-based formulation. Compos Struct 255:112969
74. Phung-Van P, Thai CH, Nguyen-Xuan H, Abdel-Wahab M (2019) An isogeometric approach of static and free vibration analyses for porous FG nanoplates. Eur J Mech A Solids 78:103851
75. Yang F, Chong ACM, Lam DCC et al (2002) Couple stress based strain gradient theory for elasticity. Int J Solids Struct 39:2731–2743
76. Eringen AC (1972) Linear theory of nonlocal elasticity and dispersion of plane waves. Int J Eng Sci 10:425–435
77. Thai CH, Ferreira AJM, Abdel Wahab M, Nguyen-Xuan H (2016) A generalized layerwise higher-order shear deformation theory for laminated composite and sandwich plates based on isogeometric analysis. Acta Mech 227:1225–1250
78. Nguyen TN, Ngo TD, Nguyen-Xuan H (2017) A novel three-variable shear deformation plate formulation: theory and Isogeometric implementation. Comput Methods Appl Mech Eng 326:376–401
79. Phung-Van P, Tran LV, Ferreira AJM, Nguyen-Xuan H, Abdel-Wahab M (2017) Nonlinear transient isogeometric analysis of smart piezoelectric functionally graded material plates based on generalized shear deformation theory under thermo-electro-mechanical loads. Nonlinear Dyn 87:879–894
80. Mou B, Li X, Bai Y, Wang L (2019) Shear behavior of panel zones in steel beam-to-column connections with unequal depth of outer annular stiffener. J Struct Eng 145:04018247
81. Fang W, Yu T, Lich LV, Bui TQ (2019) Analysis of thick porous beams by a quasi-3D theory and isogeometric analysis. Compos Struct 221:110890
82. Huang ZQ, Yi SH, Chen HX, He XQ (2019) Parameter analysis of damaged region for laminates with matrix defects. J Sandwich Struct Mater. https://doi.org/10.1177/1099636219842290
83. Thanh C-L, Ferreira AJM, Abdel-Wahab M (2019) A refined size-dependent couple stress theory for laminated composite micro-plates using isogeometric analysis. Thin Walled Struct 145:106427
84. Thanh C-L, Tran LV, Bui TQ, Nguyen HX, Abdel-Wahab M (2019) Isogeometric analysis for size-dependent nonlinear thermal stability of porous FG microplates. Compos Struct 221:110838
85. Nguyen TN, Thai CH, Luu A-T, Nguyen-Xuan H, Lee J (2019) NURBS-based postbuckling analysis of functionally graded carbon nanotube-reinforced composite shells. Comput Methods Appl Mech Eng 347:983–1003
86. Gholipour G, Zhang C, Mousavi AA (2020) Numerical analysis of axially loaded RC columns subjected to the combination of impact and blast loads. Eng Struct 219:110924
87. Sun L, Yang Z, Jin Q, Yan W (2020) Effect of axial compression ratio on seismic behavior of GFRP reinforced concrete columns. Int J Struct Stab Dyn 20:2040004
88. Qiu J, Sahmani S, Safaei B (2020) On the NURBS-based isogeometric analysis for couple stress-based nonlinear instability of PFGM microplates. Mech Based Design Struct Mach. https://doi.org/10.1080/15397734.2020.1853567
89. Miller RE, Shenoy VB (2000) Size-dependent elastic properties of nanosized structural elements. Nanotechnology 11:139–147
90. Singh G, Rao GV, Iyengar NGR (1994) Geometrically nonlinear flexural response characteristics of shear deformable unsymmetrically laminated plates. Comput Struct 53:69–81